

# Dense gas tracing the collisional past of Andromeda

## An atypical inner region?

Anne-Laure Melchior<sup>1,2</sup>, Françoise Combes<sup>1,3</sup>

<sup>1</sup> LERMA, Observatoire de Paris, PSL Research University, CNRS, UMR 8112, F-75014, Paris France  
e-mail: A.L.Melchior@obspm.fr, Francoise.Combes@obspm.fr

<sup>2</sup> Sorbonne Universités, UPMC Univ. Paris 6, UMR 8112, LERMA, F-75005, Paris, France

<sup>3</sup> Collège de France, 11, Place Marcelin Berthelot, F-75 005 Paris, France

Received April 3, 2015; accepted

### ABSTRACT

The central kiloparsec region of the Andromeda galaxy is relatively gas poor, while the interstellar medium appears to be concentrated in a ring-like structure at about 10 kpc radius. The central gas depletion has been attributed to a possible head-on collision 200 Myr ago, supported by the existence of an offset inner ring of warm dust. We present new IRAM-30m observations of the molecular gas in the central region, and the detection of CO and its isotopes  $^{13}\text{CO}(2-1)$  and  $\text{C}^{18}\text{O}(2-1)$ , together with the dense gas tracers,  $\text{HCN}(1-0)$  and  $\text{HCO}^+(1-0)$ . A systematic study of the observed peak temperatures with non-LTE equilibrium simulations shows that the detected lines trace dense regions with  $n_{\text{H}_2}$  in the range  $2.5 \times 10^4 - 5.6 \times 10^5 \text{ cm}^{-3}$ , while the gas is very clumpy with a beam filling factor of  $0.5 - 2 \times 10^{-2}$ . We also show that the gas is optically thin in all lines, except the  $^{12}\text{CO}(1-0)$  and  $^{12}\text{CO}(2-1)$  lines, that the CO lines are close to the thermal equilibrium at 17.5-20 K and a molecular hydrogen density larger than critical and that the HCN and HCO+ lines have a subthermal excitation temperature of 8-10 K with a density smaller than critical. The molecular mass we derive is compatible with the dust mass derived from the far-infrared emission, assuming a dust-to-gas mass ratio of 0.01. In one of the regions, the  $^{12}\text{CO}/^{13}\text{CO}$  line ratio is quite high ( $\sim 20$ ), and equals to the  $^{12}\text{CO}/\text{C}^{18}\text{O}$  ratio. The fact that the optically thin  $^{13}\text{CO}$  and  $\text{C}^{18}\text{O}$  lines have comparable intensities means that the secondary element  $^{13}\text{C}$  is depleted with respect to the primary  $^{12}\text{C}$ , as is expected just after a recent star formation. This suggests that there has been a recent starburst in the central region, supporting the head-on collision scenario.

**Key words.** galaxies: abundances; galaxies: individual: M31; galaxies: kinematics and dynamics; submillimeter: ISM; molecular data

## 1. Introduction

While the outer parts of the Andromeda galaxy exhibit numerous relics of past interactions (McConnachie et al. 2009), the main disc focuses star formation activity in a ring at 10 kpc (Ford et al. 2013) and the central part is atypical. It hosts a very massive black hole with a mass of  $0.7 - 1.4 \times 10^8 M_\odot$  (Bacon et al. 2001; Bender et al. 2005), which is one of the most underluminous super-massive black hole (Garcia et al. 2010), surrounded by very little gas (Melchior & Combes 2013). Infrared data and optical ionised gas display a 0.7 kpc off-centred inner ring, and Block et al. (2006) have proposed a frontal collision with M32 to explain this double ring structure. It would have occurred 200 Myr ago. In this paper, we present observations of millimetre molecular lines probing dense gas regions along the minor axis in the inner ring. As first discussed in Melchior & Combes (2011), we also detect several velocity components. In Section 2, we present the data used in this paper. In Section 3, we describe the data reduction. In Section 4, we describe our

results and which physical information we can extract. In Section 5, we argue that our results support a 200 Myr old starburst triggered by the frontal collision with M32. For consistency with our previous analysis, we consider a distance of M31 of 780 kpc and a pixel size 1 arcsec = 3.8 pc.

## 2. The data

### 2.1. Millimetre observations

We observed five positions provided in Table 1, which also gives the offsets computed with respect to the position of the optical centre ( $00^{\text{h}}42^{\text{m}}44.371^{\text{s}} +41^\circ16'08.34''$ ) provided by Crane et al. (1992) and used in previous papers (Melchior et al. 2000; Melchior & Combes 2011, 2013) and the integration time. The observed positions lie in the inner 1-kpc ring along the minor axis (of the main disc inclined at 77 deg). The total integration time for each position is provided in the last column. These positions have been superimposed on the Herschel 100  $\mu\text{m}$

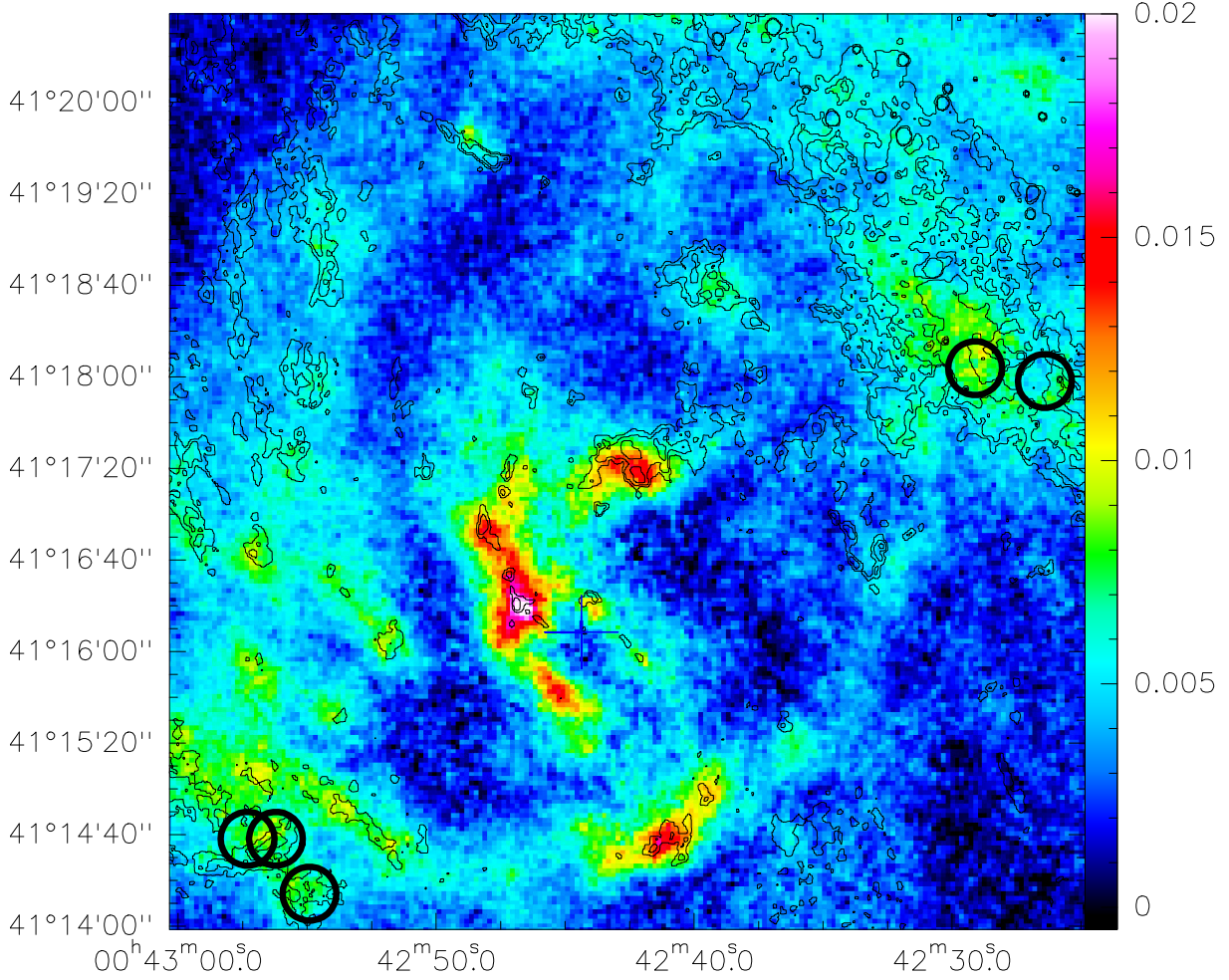


**Fig. 1.** Positions observed in HCO+(1-0), HCN(1-0) and  $^{13}\text{CO}(2-1)$  (and  $\text{C}^{18}\text{O}$ ) are indicated by circles superimposed on the PACS/Herschel 100 $\mu\text{m}$  map (Viaene et al. 2014) and the contour levels (0.05 0.1 0.2) correspond  $A_B$  extinction computed assuming all the dust is in front of the bulge as discussed in Melchior et al. (2000). Extinction is underestimated by an unknown factor due to the uncertainties on the geometrical configuration of the gas in this area.

**Table 1.** M31 observed positions. We provide the J2000 coordinates, offsets and integration times of the five positions observed.

Pos	RA (J2000)	DEC (J2000)	$\Delta\alpha$ (")	$\Delta\delta$ (")	$T_{\text{int}}$ (min)
I	00 42 29.1	+41 18 03.6	-172.1	115.3	284
I-B	00 42 26.4	+41 17 58.0	-202.5	109.7	173
2d-a	00 42 56.2	+41 14 38.0	133.4	-90.3	262
2d-b	00 42 57.3	+41 14 38.0	145.8	-90.3	204
2c-a	00 42 54.9	+41 14 14.0	118.8	-114.3	79

map provided by Viaene et al. (2014) (and  $A_B$  extinction contours computed in Melchior et al. (2000)) in Figure 1. In the 100 $\mu\text{m}$  and  $A_B$  maps, we can see the 0.7 kpc off-centred inner ring.

The observations have been performed with the IRAM-30m radiotelescope equipped with the EMIR receiver in the period 20<sup>th</sup>-23<sup>rd</sup> December 2011. They were

performed in dual polarisation and the E0/E2 band combination have been tuned in order to cover the following frequency bandwidths:

1. 87.4-91.4 GHz and 83.8-87.8 GHz (optimised for HCO+(1-0) and HCN(1-0))
2. 218.65-222.65 GHz and 214.95-218.95 GHz (optimised for  $^{13}\text{CO}(2-1)$  and  $\text{C}^{18}\text{O}$ ).

Two backends have been connected to two main receivers: FTS with a spectral resolution of 0.19 MHz and WILMA autocorrelator with a spectral resolution of 2 MHz. WILMA has been non-operational in some observations, and have been mainly used to check the quality of the observations. FTS data have been smoothed to the optimised resolution of 2.1 km s<sup>-1</sup> up to 34 km s<sup>-1</sup>. Observations have been performed in non-symmetric wobbler mode, in order to avoid sky subtraction from Andromeda's main disc. The azimuthal radius of the wobb-



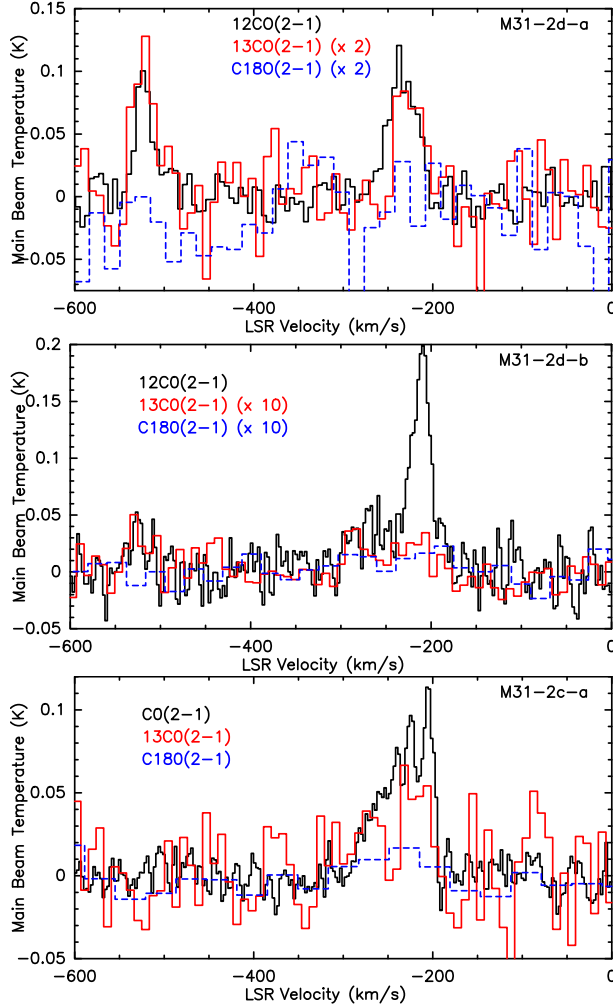


**Fig. 5.** Carbon monoxide spectra observed in the South-East side of the inner ring are superimposed in velocity. The main beam temperature is provided for  $^{12}\text{CO}$ , while the  $^{13}\text{CO}$  and  $\text{C}^{18}\text{O}$  spectra are multiplied by a factor of 10.

been extracted from the work of Viaene et al. (2014) and Draine et al. (2014). They are summarised in Table 2.

Draine et al. (2014) has adjusted a physical dust model on Herschel and Spitzer observations to estimate the mean intensities of starlight heating the dust. They have been computed for the SPIRE 350/Herschel and MIPS 160/Spitzer resolutions respectively  $24.''9$  and  $39.''$ . The latter accounts for 2 more photometric channels. The mean starlight recovered for both resolutions are provided in the second and third columns of Table 2. These differences have an amplitude comparable to the 30% discrepancy between the inferred heating rate and the value predicted by a simple model of bulge starlight discussed by Draine et al. (2014). This gives an idea of the real uncertainty of these estimates, that smooth the substructures, while the corresponding resolutions ( $24.''9$  and  $39.''$ ) are comparable and larger than those of our millimeter ob-

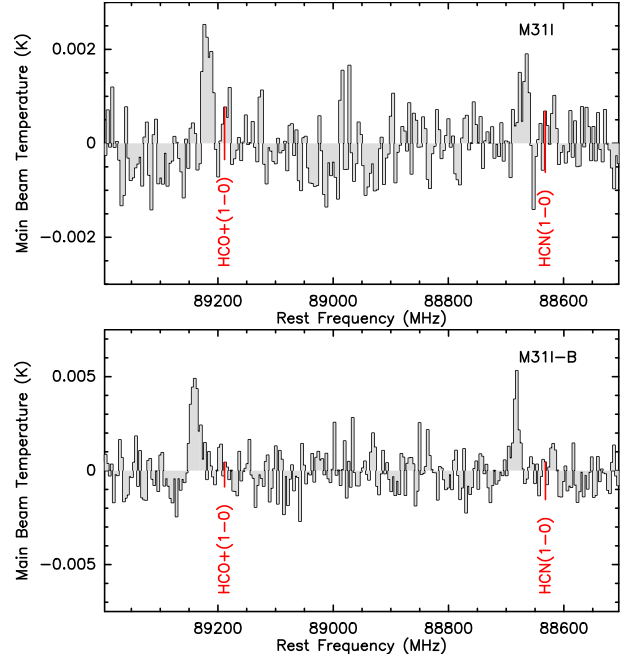


**Fig. 6.** Signal detected in  $\text{HCO}^+(1-0)$  and  $\text{HCN}(1-0)$ . The main-beam temperatures are displayed as a function of the rest-frame frequency of the Andromeda galaxy (corresponding to  $-300\text{km s}^{-1}$ ).

servations ( $11''$ ,  $21''$  and  $28''$ , see Table 2). We then provide the cold dust temperatures computed according to the Draine & Li (2007) model as  $T_{\text{dust}}^{\text{cold}} = T^{1/6}$ . In the studied area, Draine et al. (2014) find that the starlight heating intensity is compatible with the stars in the bulge, as found by Groves et al. (2012). Relying on Herschel data, as well as GALEX, SDSS, WISE and Spitzer, Viaene et al. (2014) have modelled the spectral energy distribution to extract physical quantities. They have estimated cold dust temperatures, which are similar to those derived from Draine et al. (2014), as displayed in Table 2. The differences could be accounted for by the different datasets used as well as the different modelling, Viaene et al. (2014) are directly fitting the spectral energy distribution, while Draine et al. (2014) relying on a physical model. They have also provided a warm dust temperature (labelled "birth cloud" in their paper) larger than in the surrounding regions. This suggests that there are substructures linked to recent star formation, corresponding to a (weak) star-forming activity ( $3\text{-}15\text{M}_{\odot}/\text{Myr}$ ). We can expect the kinetic temperatures to be equal at most to the dust temperature, depending on the molecular hydrogen density. In the following, we will consider a kinetic temperature of 20 K, which corresponds to the cold gas temperature.

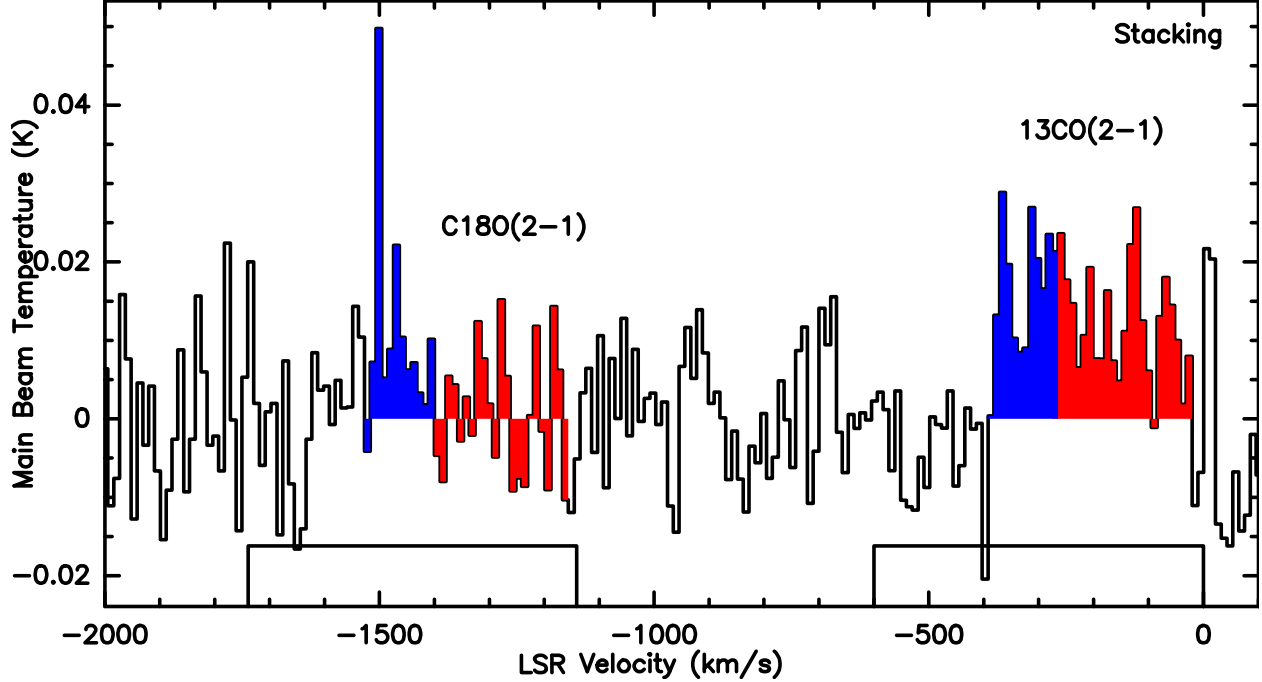


**Fig. 7.** Stacking with centring at the systemic velocity of each  $^{13}\text{CO}(2-1)$  detections. This reveals a blue component in  $\text{C}^{18}\text{O}(2-1)$ , with an amplitude comparable with the corresponding  $^{13}\text{CO}(2-1)$ , while there is no corresponding red component. The blue and red surfaces, displayed in the two lines, correspond to the same velocity range.

### 3. Data reduction

The CLASS<sup>1</sup> package was used for the reduction. Individual spectra have been inspected before averaging with a weight proportional to the exposure time.

Various interference lines are present far from the expected astronomical signals, but they are affecting the determination of the baselines. They have been carefully removed on each spectra. The M31I position has suffered an interference next to the strongest peak of the  $^{13}\text{CO}(1-0)$  line. It affects only the data acquired on 20<sup>th</sup> December 2011 (18/30). We thus set to zero the corresponding channels on data taken with the FTS backend with the best spectral resolution ( $0.26 \text{ km s}^{-1}$ ).

The observations averaged in the two main bandwidths are presented in the Figures 2 and 3. These spectra reveal multicomponent signals corresponding to the Andromeda velocity range (given its systemic velocity of  $-300 \text{ km s}^{-1}$ ).

Characteristics of the main astronomical molecular lines (Schöier et al. 2005) present in the observed bandwidths are provided in Table 3: the half power beam width (HPBW), the beam efficiency, the restframe frequency and the velocity bin corresponding to 14 MHz. We also provide the characteristics of these molecules: the energy level, the Einstein coefficient  $A_{ul}$ , the collisional de-excitation rate  $C_{ul}$  and the critical density  $n_c$  computed at 20 K. If we consider a collisional temperature of 50 K, the

critical densities of HCN and HCO+ increase respectively by 56% and 21%, but by 7.4% for CO. There are obvious detections of HCO+(1-0), HCN(1-0) and  $^{13}\text{CO}(2-1)$  in the summed spectra, and a weak signal in  $\text{C}^{18}\text{O}(2-1)$ . There is obviously no contamination from the Milky Way, which could be possible as M31 is 20 deg below the Galactic plane. The spectra obtained in the Lower Outer bands are presented in Figure A.1 but do not exhibit any signal. They are used to derived upper limits. For each position, the detections are adjusted with a Gaussian function. Up to three different CO lines are detected at different central velocity at each position. As discussed in Melchior & Combes (2011), this is due to several intervening molecular components along the line of sight.

All the measurements are summarised in Table 4. The columns on the right side provides the CO line measurements. We provide for each CO line the central LSR velocity, the FWHM velocity dispersion  $\Delta v$ , the peak (main-beam) temperature  $T_{\text{peak}}$ , and the integral  $I_{\text{CO}}$  of the line. We also provide the column densities  $N_{\text{H}_2}$  of molecular hydrogen relying on  $X_{\text{CO}}$  and  $\text{CO}(2-1)/(1-0)$  line ratio values. We assume a Galactic ratio  $X_{\text{CO}} = N_{\text{H}_2}/I'_{\text{CO}} = 2. \times 10^{20} \text{ cm}^{-2} (\text{K km s}^{-1})^{-1}$  following Strong et al. (1988) and Dame et al. (2001), which is compatible with the findings of Smith et al. (2012) for Andromeda and Mauersberger et al. (2003) for local galaxies. As further discussed in Section 4.3, we take  $I'_{\text{CO}} = I_{\text{CO}}/\eta_{\text{bf}}$ . We assume a  $\text{CO}(2-1)/(1-0)$  line ratio of 0.8, as measured by Melchior & Combes (2011) in a clump located within  $10''$  of M31I (and named M31G), to compute  $N_{\text{H}_2}$  col-

<sup>1</sup> Continuum and Line Analysis Single-dish Software, <http://www.iram.fr/IRAMFR/GILDAS>



umn densities. In the last two columns, the  $^{12}\text{CO}/^{13}\text{CO}(2-1)$  and  $^{12}\text{CO}/\text{C}^{18}\text{O}(2-1)$  line ratios and lower limits are displayed. We also provide (in the bottom of this table) our  $^{12}\text{CO}(1-0)$  measurements described in Melchior & Combes (2011) for M31-I with a beam resolution of 21 arcsec, similar to the resolution achieved for HCN(1-0) and HCO+(1-0).

The columns on the left side gathers HCN(1-0) and HCO+(1-0) measurements and  $3\sigma$  upper limits (for  $\Delta v=32 \text{ km s}^{-1}$ ) for some lines presented in Table 3. The central table provides the remaining upper limits, as well as column densities (and upper limits) of the species with some detections, namely  $^{13}\text{CO}$ ,  $\text{C}^{18}\text{O}$ , HCN and HCO+, assuming Local Thermal Equilibrium (LTE) and optically thin conditions. The column densities have been corrected for the beam filling factor, as further discussed in the next section. Given the velocity dispersion of the observed HCN lines ( $>25 \text{ km s}^{-1}$ ), the HCN hyperfine line structure ( $\sim 10 \text{ km s}^{-1}$ ) will not be detected.

## 4. Results

### 4.1. Description of the detections

The CO lines detected in the North-West (resp. South-East) region are displayed in Figure 4 (resp. 5). The HCN(1-0) and HCO+(1-0) lines detected in the North-West side are shown in Figure 6.

As shown in Table 4, up to 5 different molecular lines (2 to 4 per position and per velocity component) have been detected. For some positions (M31I, M31I-B, M31-2d-a), there are clearly several well-identified peaks with different velocities, while for other positions the signal is very wide and best fitted with several components: the most striking cases are M31-2c-a, and the low-velocity component of M31-2d-b. Beside the  $^{12}\text{CO}$  and some  $^{13}\text{CO}$  lines, the detections are weak with peak temperatures at the mK level. To be noted the  $\text{C}^{18}\text{O}$  detection is at a level comparable to the  $^{13}\text{CO}$  detection. While  $^{12}\text{CO}$  and  $^{13}\text{CO}$  are detected on both regions,  $\text{C}^{18}\text{O}$ , HCN(1-0) and HCO+(1-0) are only detected in the North-West side. If the dust-to-gas mass ratio is similar on both sides, we expect according to Viaene et al. (2014) a gas mass a factor of 3 larger on this side (see Table 2). Similarly, when one averages the observed column densities of molecular hydrogen provided in Table 4 along the two lines of sight, the North-West positions have a column density a factor of 2 higher than the South-East ones. Also, the radiation field ( $U$ ) is larger in the South-East side than in the North-West side: this may be related to larger CO column densities and to the fact that dense gas ( $\text{C}^{18}\text{O}$ , HCN, HCO+) is not detected in the South-East positions.

The  $\text{C}^{18}\text{O}$  detection corresponds to the component at the systemic velocity, while the HCN and HCO+ detections are in the blueshifted components. However, as displayed in Figure 7, stacking of the  $^{13}\text{CO}$  detections, also reveals a blueshifted component in  $\text{C}^{18}\text{O}$  with an amplitude comparable with  $^{13}\text{CO}$ . The characteristics of this stacking detection is presented in Table 6. The  $^{13}\text{CO}/\text{C}^{18}\text{O}$

line ratio is close to 1. We thus have at least two different  $\text{C}^{18}\text{O}$  components at two different velocities.

The difficulty of the interpretation of these dense gas detections is due to a complicated configuration. We are integrating the signal over a relatively large beam (42-106 pc in projection), and the velocity dispersions ( $>25 \text{ km/s}$ ) we detect here are significantly larger than the ones ( $\sim 2 \text{ km/s}$ ) detected in M31's main disc (Schruba et al., in prep). This is due to the strong velocity gradient present in this region and to the superposition of several clouds.

### 4.2. Observed line ratios

When one computes line ratios based on velocity-integrated intensities as displayed in Table 5, it is striking to note that the  $^{13}\text{CO}$  and  $\text{C}^{18}\text{O}$  intensities are at the same level. As displayed in Figure 8, our measured  $^{13}\text{CO}/\text{C}^{18}\text{O}(2-1)$  line ratios lie below the (1-0) measurements of Liu et al. (2014) in infrared Galactic dark clouds (average  $4.4 \pm 1.3$ , see their Figure 2), but corresponds to the lower end of the Tan et al. (2011) starburst sample distribution based on  $^{13}\text{CO}/\text{C}^{18}\text{O}(1-0)$  line ratio. It is also significantly lower than the M51's spiral arms gas detected by Schinnerer et al. (2010) (their average  $^{13}\text{CO}/\text{C}^{18}\text{O}$  line ratio: 3.5).

As displayed in Figure 7, stacking of the  $^{13}\text{CO}$  detections exhibit a clear signal in the blueshifted component in  $\text{C}^{18}\text{O}$  with an amplitude also comparable with  $^{13}\text{CO}$ . In addition, there is some very low velocity dispersion clumps which appears (they have been smoothed for the figure). It corresponds to the expected CO gas distribution, with the  $\text{C}^{18}\text{O}$  gas more clumpy than the  $^{13}\text{CO}$  component. This supports the characteristics of our single  $\text{C}^{18}\text{O}$  detection (close to the systemic velocity), with a relative  $^{13}\text{CO}/\text{C}^{18}\text{O}$  deficit.  $^{13}\text{CO}/\text{C}^{18}\text{O}$  line ratios close to one are expected if  $^{13}\text{CO}$  is optically thick or if  $^{13}\text{C}$  is depleted with respect to  $^{12}\text{C}$  like after a starburst. As further discussed in Sect. 4.4,  $^{13}\text{CO}$  is optically thin, so the post-starburst solution is probably more appropriate. Such a  $^{13}\text{CO}$  deficit was first observed by Casoli et al. (1991) in post-merger. The  $^{13}\text{CO}$  is under-abundant with respect to  $\text{C}^{18}\text{O}$ . Davis, T. A. (2014) also find an anticorrelation of  $^{13}\text{CO}$  and the star formation and gas surface densities in local galaxies. This could be the signature of a 200 Myr old starburst triggered by a collision with a galaxy like M32, as proposed by Block et al. (2006).

In Figure 9, we compare our  $^{12}\text{CO}/^{13}\text{CO}(2-1)$  line ratios with values measured previously in other galaxies. We consider the following catalogues:

- the (2-1) line ratio compilations for different morphological types from Krips et al. (2010). We provide the different morphological types under the form of hatched histogram.
- the (1-0) line ratio measured by Li et al. (2014) in nearby galaxies.
- the (1-0) line ratio measured by Matsushita et al. (2010) in starburst and poststarburst galaxies.

**Table 3.** Properties of the main lines in the two observed bands. The beam sizes (HPBW) and the main beam efficiencies ( $\eta_{mb}$ ) are presented together with the rest frequencies  $\nu_0$  of the brightest lines in each band and the velocity bin corresponding to 1 MHz. The energy levels  $E_{up}$  and the Einstein coefficient  $A_{ul}$  are based on the Leiden Atomic and Molecular Database (Schöier et al. 2005), as well as the collisional de-excitation rate coefficients  $C_{ul}$  computed at a kinetic temperature of 20 K. The critical density is computed as  $n_c = A_{ul}/C_{ul}$ .

Transition	HPBW (arcsec)	$\eta_{mb}$	$\nu_0$ (GHz)	$\delta v$ (1 MHz) (km s <sup>-1</sup> )	$E_{up}$ (K)	$A_{ul}$ s <sup>-1</sup>	$C_{ul}$ (cm <sup>3</sup> s <sup>-1</sup> )	$n_c$ (20 K) (cm <sup>-3</sup> )
SiO $J = 2 \rightarrow 1$	28.	81	86.847	3.5	6.25	$2.93 \cdot 10^{-5}$	$1.1 \cdot 10^{-10}$	$2.93 \cdot 10^5$
C <sub>2</sub> H N = 1 $\rightarrow$ 0 ( $J = 3/2 \rightarrow 1/2, F = 1 - 1$ )	28.	81	87.329	3.4	4.19	$0.26 \cdot 10^{-6}$	$5.19 \cdot 10^{-12}$	$5.01 \cdot 10^4$
HNCO( $4_{04} \rightarrow 3_{03}$ )	28.	81	87.925	3.4	10.55	$9.02 \cdot 10^{-6}$	$9.2 \cdot 10^{-12}$	$9.80 \cdot 10^5$
HCN $J = 1 \rightarrow 0$	28.	81	88.632	3.4	4.25	$2.41 \cdot 10^{-5}$	$1.92 \cdot 10^{-11}$	$1.26 \cdot 10^6$
HCO <sup>+</sup> $J = 1 \rightarrow 0$	28.	81	89.189	3.4	4.28	$4.25 \cdot 10^{-5}$	$2.3 \cdot 10^{-10}$	$1.85 \cdot 10^5$
HNC $J = 1 \rightarrow 0$	27.	81	90.664	3.3	4.35	$2.69 \cdot 10^{-5}$	$8.95 \cdot 10^{-11}$	$3.01 \cdot 10^5$
HC <sub>3</sub> N $J = 10 \rightarrow 9$	27.	81	90.979	3.3	24.01	$5.81 \cdot 10^{-5}$	$1.1 \cdot 10^{-10}$	$5.28 \cdot 10^5$
SiO $J = 5 \rightarrow 4$	11.	60	217.105	1.4	31.26	$5.20 \cdot 10^{-4}$	$1.1 \cdot 10^{-10}$	$4.73 \cdot 10^6$
H <sub>2</sub> CO( $3_{03} \rightarrow 2_{02}$ )	11.	60	218.222	1.4	21.0	$2.82 \cdot 10^{-4}$	$1.1 \cdot 10^{-10}$	$2.56 \cdot 10^6$
H <sub>2</sub> CO( $3_{22} \rightarrow 2_{21}$ )	11.	60	218.476	1.4	68.1	$1.57 \cdot 10^{-4}$	$5.3 \cdot 10^{-11}$	$2.96 \cdot 10^6$
H <sub>2</sub> CO( $3_{21} \rightarrow 2_{20}$ )	11.	60	218.760	1.4	68.1	$1.58 \cdot 10^{-4}$	$4.3 \cdot 10^{-11}$	$3.67 \cdot 10^6$
C <sup>18</sup> O $J = 2 \rightarrow 1$	11.	60	219.560	1.4	15.81	$6.01 \cdot 10^{-7}$	$6.44 \cdot 10^{-11}$	$9.33 \cdot 10^3$
<sup>13</sup> CO $J = 2 \rightarrow 1$	11.	60	220.399	1.4	15.87	$6.04 \cdot 10^{-7}$	$6.44 \cdot 10^{-11}$	$9.38 \cdot 10^3$
<sup>12</sup> CO $J = 2 \rightarrow 1$	11.	60	230.538	1.3	16.60	$6.91 \cdot 10^{-7}$	$6.44 \cdot 10^{-11}$	$1.07 \cdot 10^4$
<sup>12</sup> CO $J = 1 \rightarrow 0$	21.	71	115.271	2.6	5.53	$7.20 \cdot 10^{-8}$	$3.25 \cdot 10^{-11}$	$2.22 \cdot 10^3$

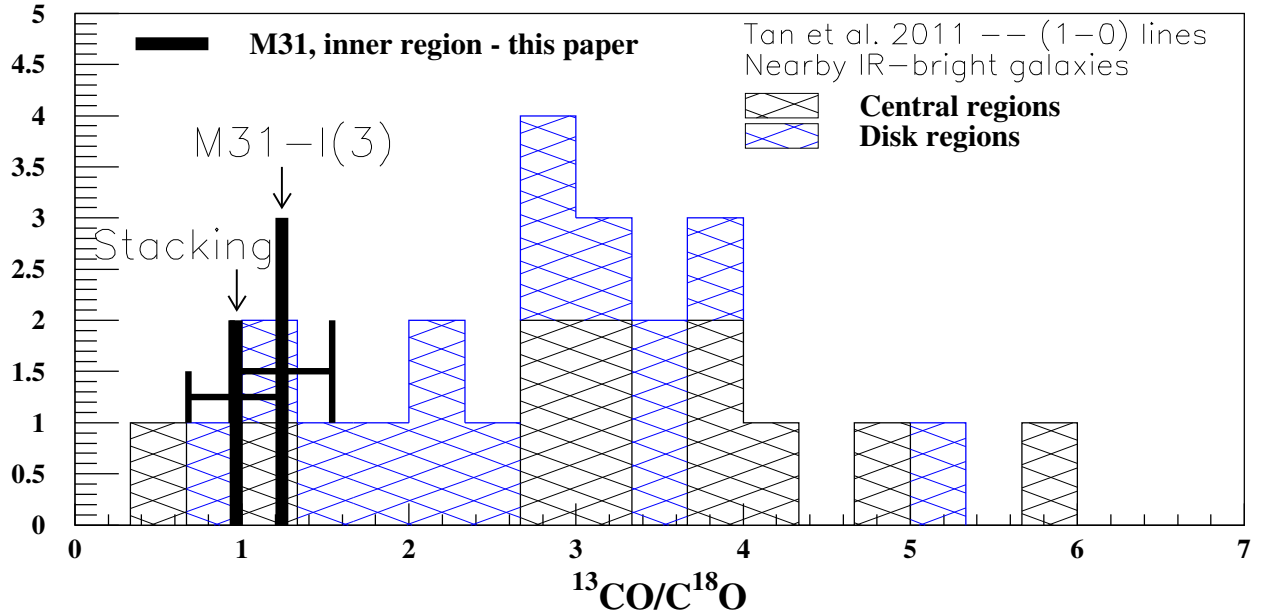


**Fig. 8.** Comparison of our  $^{13}\text{CO}/\text{C}^{18}\text{O}(2-1)$  line ratio measurements (M31-I(3) and stacking) corresponding to different clouds (i.e. with different velocities) with previous measurements in nearby galaxies from Tan et al. (2011). The hatched histogram displayed the original  $^{13}\text{CO}/\text{C}^{18}\text{O}(1-0)$  line ratio.

- the (1-0) line ratio measured by Tan et al. (2011) in nearby infrared-bright galaxies and starbursts.

The (1-0) line ratios have been corrected with the average  $^{12}\text{CO}/^{13}\text{CO}(1-0)/(2-1)$  ratio (1.33) from Krips et al. (2010). The hatched histogram displays the different morphological types when available: no clear effect linked to the morphology appears. As discussed by Li et al. (2014),

the isotopologue ratio does not depend on the morphological type of the galaxy. Our measurements (with an average  $^{12}\text{CO}/^{13}\text{CO} = 18$ ) lie below the standard isotopic ratio (53) (Wilson & Rood 1994) but fall in the same range as the other measurements. This is consistent with the fact that  $^{12}\text{CO}$  is optically thick. Due to very different observational configurations, it is difficult to compare with Galactic regions. For instance, Orion regions observed by

**Table 4.** Results. *Right:* CO(2-1) line fit results.  $I_{CO}$  upper limits are provided at  $3\sigma$ . The hydrogen column density have been computed as discussed in Sect. 3 with a Galactic  $X_{CO}$  factor. *Middle:*  $3\sigma$  upper limits on molecular lines observed in the LO (Lower Outer) band (with  $\sigma = 32\text{km/s}$ ). Column densities of the main molecules corrected for beam-filling factors. *Left:* HCO+(1-0) and HCN(1-0) Line fit results. HNC(1-0), HNCO(4-3), HOC+(1-0) and HC3N(10-9) upper limits are provided at  $3\Delta v$  (assuming  $\sigma = 32\text{km/s}$ ).

Pos.	V <sub>0</sub> (km/s)			Δv (km/s)			T <sub>peak</sub> (mK)			I <sub>line</sub> (K km s <sup>-1</sup> )			N <sub>H<sub>2</sub></sub>	I <sub>2CO</sub> /I <sub>3CO</sub>	I <sub>2CO</sub> /I <sub>C<sup>18</sup>O</sub>
	<sup>12</sup> CO	<sup>13</sup> CO	C <sup>18</sup> O	<sup>12</sup> CO	<sup>13</sup> CO	C <sup>18</sup> O	<sup>12</sup> CO	<sup>13</sup> CO	C <sup>18</sup> O	<sup>12</sup> CO	<sup>13</sup> CO	C <sup>18</sup> O			
(2-1)	-144.2±0.2	-144.6±0.7	-402*	7.5±0.5	9.±2	422	18.6	3.4±0.2	0.17±0.03	<0.057	2.9±0.2	20.±4	>59.6	>45.7	>45.7
I(1)	-402.±3	-402*	-291*	62±12	62*	146	4.6	9.6±0.5	0.30±0.06	<0.21	24.2±1.3	32.±7	>45.7	>45.7	>45.7
I(2)	-291.±9	-291*	-463*	69±18	69*	77	4.9	6±1	0.36±0.06	0.29±0.07	28.8±4.8	17±4	>45.7	>45.7	>45.7
I-B(1)	-463.0±0.7	-463*	-291*	38±2	38*	356	11.1	14.3±0.6	0.45±0.04	<0.10	38.4±1.6	32.±3.	>143	>143	>143
I-B(2)	-397.±7	-397*	-291*	66±14	66*	49.2	4.2	3.5±0.7	0.30±0.05	<0.51	51.5±10.3	12.±3.	>6.9	>6.9	>6.9
2d-a(1)	-523.0±0.9	-522±3	-226±4	21.±3	24±6	99.8	5.8	2.2±0.2	0.15±0.03	<0.13	8.2±0.6	15.±3	>16.9	>16.9	>16.9
2d-a(2)	-234.±1	-226±4	-211*	37.±3	36±9	105	4.9	4.1±0.3	0.19±0.04	<0.17	14.4±1.1	22.±5	>24.1	>24.1	>24.1
2d-b(1)	-211.5±0.7	-211*	-269*	30±2	30*	176	3.2	5.5±0.3	0.10±0.03	<0.06	11.5±0.6	55.0±17	>91.7	>91.7	>91.7
2d-b(2)	-269.±3	-269*	-526*	46±6	46*	44	2.7	2.1±0.3	0.13±0.04	<0.09	17.5±2.5	16.±5	>23.3	>23.3	>23.3
2d-b(3)	-526.±2	-526*	-204.7±0.4	20±8	20*	38	4.8	0.8±0.2	0.10±0.03	<0.09	7.7±1.9	8.±3	>8.9	>8.9	>8.9
2c-a(1)	-243±3			57±4		61		3.7±0.3	<0.24	<0.30	22.6±1.8	>15.4	>12.3	>12.3	>12.3
2c-a(2)	-223.9±0.6			10±2		54		0.58±0.15	<0.09	<0.11	3.9±1.0	>6.4	>5.3	>5.3	>5.3
2c-a(3)	-204.7±0.4			12.6±0.9		98		1.31±0.15	<0.09	<0.12	5.0±0.6	>14.6	>10.9	>10.9	>10.9
(1-0)	<sup>12</sup> CO			<sup>12</sup> CO		<sup>12</sup> CO		<sup>12</sup> CO							
I(1)	-144.2±0.2			9.3±0.4		322		3.2±0.1			2.21±0.07				
I(2)	-404.2±0.9			49±3		140		7.3±0.3			14.7±0.6				
I(3)	-278±3			77±14		54		2.7±0.2			10.4±0.8				

Pos.	Molecular column densities (hypothesis: LTE, optically thin, η <sub>B</sub> , 20K)									
	I <sub>line</sub> (K km s <sup>-1</sup> )									
	SiO	CCH	SiO	H <sub>2</sub> CO	H <sub>2</sub> CO	H <sub>2</sub> CO	N <sup>13</sup> CO	N <sup>c<sup>18</sup>O</sup>	N <sup>HCO</sup>	N <sup>HCO+</sup>
	(2-1)	(1-0)	(5-4)	(3 <sub>03</sub> -2 <sub>02</sub> )	(3 <sub>22</sub> -2 <sub>21</sub> )	(3 <sub>21</sub> -2 <sub>20</sub> )	(10 <sup>16</sup> )	(10 <sup>16</sup> )	(10 <sup>13</sup> )	(10 <sup>13</sup> )
I (1)	<0.009	<0.036	<0.10	<0.13	<0.14	<0.035	0.31±0.05	<0.10	<0.51	<0.58
I (2)	<0.009	<0.036	<0.10	<0.13	<0.14	<0.035	1.58±0.32	<1.08	1.98±0.50	3.26±0.57
I (3)	<0.009	<0.036	<0.10	<0.13	<0.14	<0.035	3.62±0.60	2.83 ± 0.68	<2.83	<3.24
I-B (1)	<0.050	<0.13	<0.026	<0.062	<0.042	<0.089	2.67 ±0.22	<0.42	5.5±1.1	5.43±0.6
I-B (2)	<0.050	<0.13	<0.026	<0.062	<0.042	<0.089	11.58±1.83	<6.64	<17.3	<9.90
2d-a(1)	<0.042	<0.053	<0.035	<0.025	<0.035	<0.01	1.16±0.23	<0.45	<1.1	<0.63
2d-a(2)	<0.051	<0.045	<0.133	<0.011	<0.063	<0.01	0.43±0.13	<0.12	<5.1	<2.92
2d-b(1)	<0.051	<0.045	<0.133	<0.011	<0.063	<0.01	2.24±0.69	<0.69	<20.4	<11.7
2d-b(2)	<0.051	<0.045	<0.133	<0.011	<0.063	<0.01	2.00±0.60	<0.80	<23.6	<13.5
2d-b(3)	<0.081	<0.24	<0.19	<0.052	<0.14	<0.078	<3.03	<1.69	<5.38	<3.08
2c-a(1)	<0.081	<0.24	<0.19	<0.052	<0.14	<0.078	<1.23	<0.69	<5.97	<3.41
2c-a(2)	<0.081	<0.24	<0.19	<0.052	<0.14	<0.078	<0.71	<0.42	<3.35	<1.91
2c-a(3)	<0.081	<0.24	<0.19	<0.052	<0.14	<0.078				

Pos.	Molecular column densities (hypothesis: LTE, optically thin, η <sub>B</sub> , 20K)											
	I <sub>line</sub> (K km s <sup>-1</sup> )											
	V <sub>0</sub> (km/s)	Δv (km/s)	T <sub>peak</sub> (mK)	I <sub>line</sub> (K km s <sup>-1</sup> )								
	HCO+	HCN	HCO+	HCN	HCO+	HCN	HNC	HC3N	HOC+	HNCO		
	(1-0)	(1-0)	(1-0)	(1-0)	(1-0)	(1-0)	(1-0)	(10-9)	(1-0)	(4-3)		
I(2)	-400±5	-409±4	60±10	25±7	3.6	3.0	0.23±0.04	0.08±0.02	<0.045	<0.052	<0.056	<0.054
I-B(1)	-473±4	-471±2	65±10	32±8	5.3	6.1	0.36±0.04	0.21±0.04	<0.054	<0.065	<0.072	<0.053
2d-a							<0.03	<0.05	<0.05	<0.08	<0.07	<0.05
2d-b							<0.25	<0.48	<0.18	<0.17	<0.32	<0.42
2c-a							<0.09	<0.08	<0.08	<0.14	<0.08	<0.10

8



**Table 5.** Observed line ratios. These ratio have been computed with the velocity-integrated intensities measured within similar beams for the same component.

Position	$V_0$ (km/s)	HCO+/HCN (1-0)	HNC/HCN (1-0)	HOC+/HCO+ (1-0)	$^{12}\text{CO}/\text{HCO}+$ (1-0)	$^{12}\text{CO}/\text{HCN}$ (1-0)	$^{12}\text{CO}/^{13}\text{CO}$ (2-1)
I(2)	$\sim -402$	$2.9 \pm 0.9$	$<0.56$	$<0.24$	$32. \pm 7$	$91. \pm 15$	$32. \pm 8$
I-B(1)	$\sim -470$	$1.7 \pm 0.4$	$<0.26$	$<0.20$	$40. \pm 5$	$68. \pm 13$	$32. \pm 3$

Position	$V_0$ (km/s)	$^{12}\text{CO}/\text{C}^{18}\text{O}$ (2-1)	$^{13}\text{CO}/\text{C}^{18}\text{O}$ (2-1)	$^{12}\text{CO}/^{13}\text{CO}$ (2-1)
I(3)	$\sim -291$	$21. \pm 6$	$1.2 \pm 0.4$	$17. \pm 5$

**Table 6.** Line measurements for the stacking detection displayed in Figure 7. We present the central velocities, the velocity dispersions fixed to  $35 \text{ km s}^{-1}$ , the peak temperatures, the integrated lines and the line ratio. We also provide the mean beam filling factor with equal weights (resp. average weighted by the inverse squares uncertainties on  $I_{\text{CO}}$ ). We obtain similarly  $I_{\text{CO}} = 4.10 \pm 1.33 \text{ K km s}^{-1}$  (resp.  $I_{\text{CO}} = 3.34 \pm 0.24 \text{ K km s}^{-1}$ ), that we use together with the mean beam filling factor (resp.  $\langle \eta_{bf} \rangle = 4.13 \times 10^{-3}$ ) to derive the molecular hydrogen column density ( $N_{\text{H}_2} = 1.62 \times 10^{22}$ ). The column density of molecular hydrogen derived empirically is affected by an uncertainty of a factor about 3, while the line ratio does not depend on the weighting method.

Pos.	$V_0$ (km s $^{-1}$ )		$\Delta v$ (km s $^{-1}$ )		$T_{\text{Peak}}$ (mK)		$I_{\text{line}}$ (K km s $^{-1}$ )		Line ratio	$\langle \eta_{bf} \rangle$	$N_{\text{H}_2}$
	$^{13}\text{CO}$ (2-1)	$\text{C}^{18}\text{O}$ (2-1)	$^{13}\text{CO}$ (2-1)	$\text{C}^{18}\text{O}$ (2-1)	$^{13}\text{CO}$ (2-1)	$\text{C}^{18}\text{O}$ (2-1)	$^{13}\text{CO}$ (2-1)	$\text{C}^{18}\text{O}$ (2-1)	$^{13}\text{CO}/\text{C}^{18}\text{O}$ (2-1)		$10^{22}$ cm $^{-2}$
Stack	$-361 \pm 4$	$357 \pm 4$	$35^*$	$35^*$	28	29	$1.05 \pm 0.23$	$1.08 \pm 0.23$	$0.97 \pm 0.29$	$8.64 \times 10^{-3}$	4.84

Nishimura et al. (2015) exhibits relatively low  $^{12}\text{CO}/^{13}\text{CO}$  line ratio ( $\sim 3$ ) due to the fact that the dense clouds fill the beam and  $^{12}\text{CO}$  is very optically thick.

Figure 10 displays the HCN/HCO+(1-0) and  $^{13}\text{CO}/^{12}\text{CO}$ (2-1) ratios we measured in the components approaching us in the North-Western positions, and compares them with previous observations from the literature. Superposing our measurements on the wide range of galaxy types observed by Krips et al. (2010), we surprisingly find that our detections seem to lie on an elliptical and "starburst sequence". Our measurements seem at the detection limits of the Krips et al. (2010) sample, and we can note that they do not lie in the bulk of the distribution. It is also roughly compatible with the sequence of M33 giant molecular clouds (Buchbender et al. 2013). The HCN/HCO+ line ratio is lower and marginally compatible for one point with the average ratio computed for M31's disc by Brouillet et al. (2005), but we do not know the  $^{13}\text{CO}/^{12}\text{CO}$  line ratio in the disc region, so we cannot conclude. Again, the Galactic clouds of Nishimura et al. (2015) lies on the right hand side of this Figure and are difficult to compare.

The HCN(1-0) line detections enable us to estimate lower limits on the HCN/HNC(1-0) line ratio towards the positions in the North-Western area (M31I and M31I-B), which are respectively 1.8 and 3.9. Figure A.2 compares the HCO+/CO(1-0) and HCN/CO(1-0) line ratios detected in the North-Western side of the inner ring with other positions in M31's main disc (Brouillet et al. 2005) and with other galaxies. Our detections lie systematically above the Brouillet et al. (2005) measurements performed in M31's disc, but lies in the overall distribution of Krips

et al. (2010). Figure A.3 displays the detection and upper limits of the CO line ratios.

#### 4.3. Properties

Due to the low surface filling factor, the temperatures we have detected for  $^{12}\text{CO}$ (2-1) are well below the cosmological background. As the average  $^{12}\text{CO}/^{13}\text{CO}$  line ratio (18) is well below the standard Galactic  $^{12}\text{C}/^{13}\text{C}$  abundance ratio (53) of Wilson & Rood (1994) and the  $\text{C}^{18}\text{O}$  line intensity comparable to the  $^{13}\text{CO}$  intensity, we consider that the  $^{12}\text{CO}$  line is optically thick. As the gas is detected in emission, we can then derive a minimal excitation temperature of about 3 K from the intrinsic brightness temperature  $T_B$ , with the usual formula:

$$T_B = (f(T_{\text{ex}}) - f(T_{\text{bg}})) \times (1 - e^{-\tau}) \quad (1)$$

where

$$f(T) = \frac{\frac{h\nu}{k}}{\exp(\frac{h\nu}{kT}) - 1} \quad (2)$$

Relying on the modelling of infrared measurements, Viaene et al. (2014) and Draine et al. (2014) have estimated a cold dust temperature of order 20 K (see Table 2). Since we have measured the line ratio CO(2-1)/CO(1-0)  $\sim 0.8$  (Melchior & Combes 2011), the line is thermalised. This makes sense for cold gas in the central part of a large galaxy. Most importantly, one has to take into account the beam filling factor  $\eta_{bf}$ , which affects the intrinsic brightness temperature as follows:

$$T_B = T_{\text{peak}} / \eta_{bf} \quad (3)$$

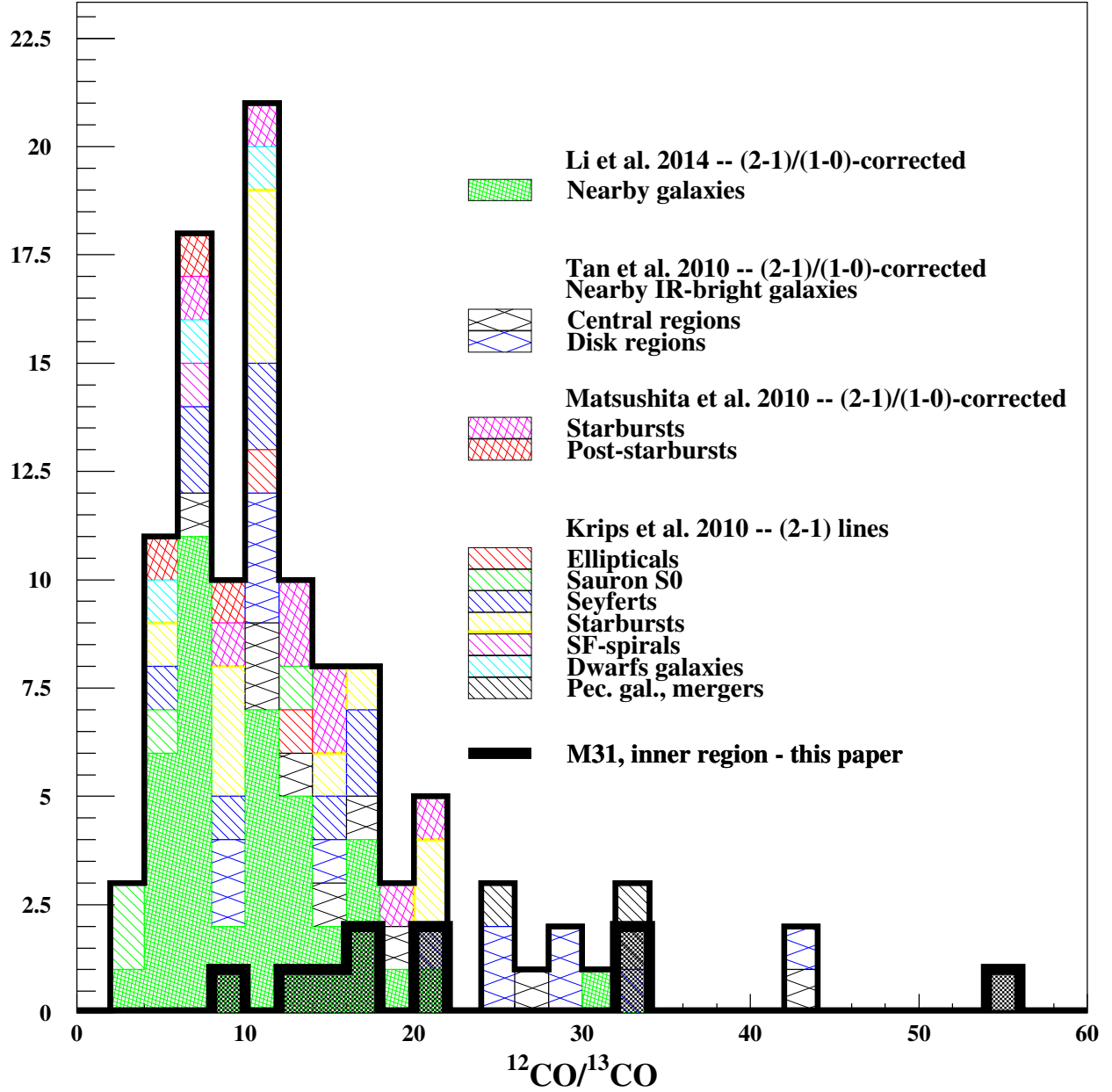


**Fig. 9.** Comparison of our  $^{12}\text{CO}/^{13}\text{CO}$  line ratio with previous measurements in nearby galaxies. The hatched histogram displayed the  $^{12}\text{CO}/^{13}\text{CO}$  line ratios with available morphological types. The Li et al. (2011), Matsushita et al. (2010) and Tan et al. (2011) samples measured the (1-0) transition and have been corrected by a factor 1.33 as discussed in the text. The Krips et al. (2010) sample and our measurements were directly measured the (2-1) transition. The black full line histogram gathers all the four samples corrected to (2-1). The black thick line histogram in the bottom corresponds to the measurements performed in this paper. The average  $^{12}\text{CO}/^{13}\text{CO}$  detected in this paper tends to be a bit larger than the main distribution from other areas and other galaxies (but well below the standard isotopic ratio of 53 (Wilson & Rood 1994)). The largest value above 50 might correspond to an optically thin cloud, but it is affected by a large error bar (30%, see Table 4).

where  $T_{\text{peak}}$  is the peak temperature measured for our detections, i.e. the observed diluted main beam temperature. Given our assumptions on the excitation temperature, we

can derive  $\eta_{bf}$  from our  $^{12}\text{CO}(2-1)$  detections as :

$$\eta_{bf} = T_{\text{peak}} / [f(T_{\text{ex}}) - f(T_{\text{bg}})] \quad (4)$$

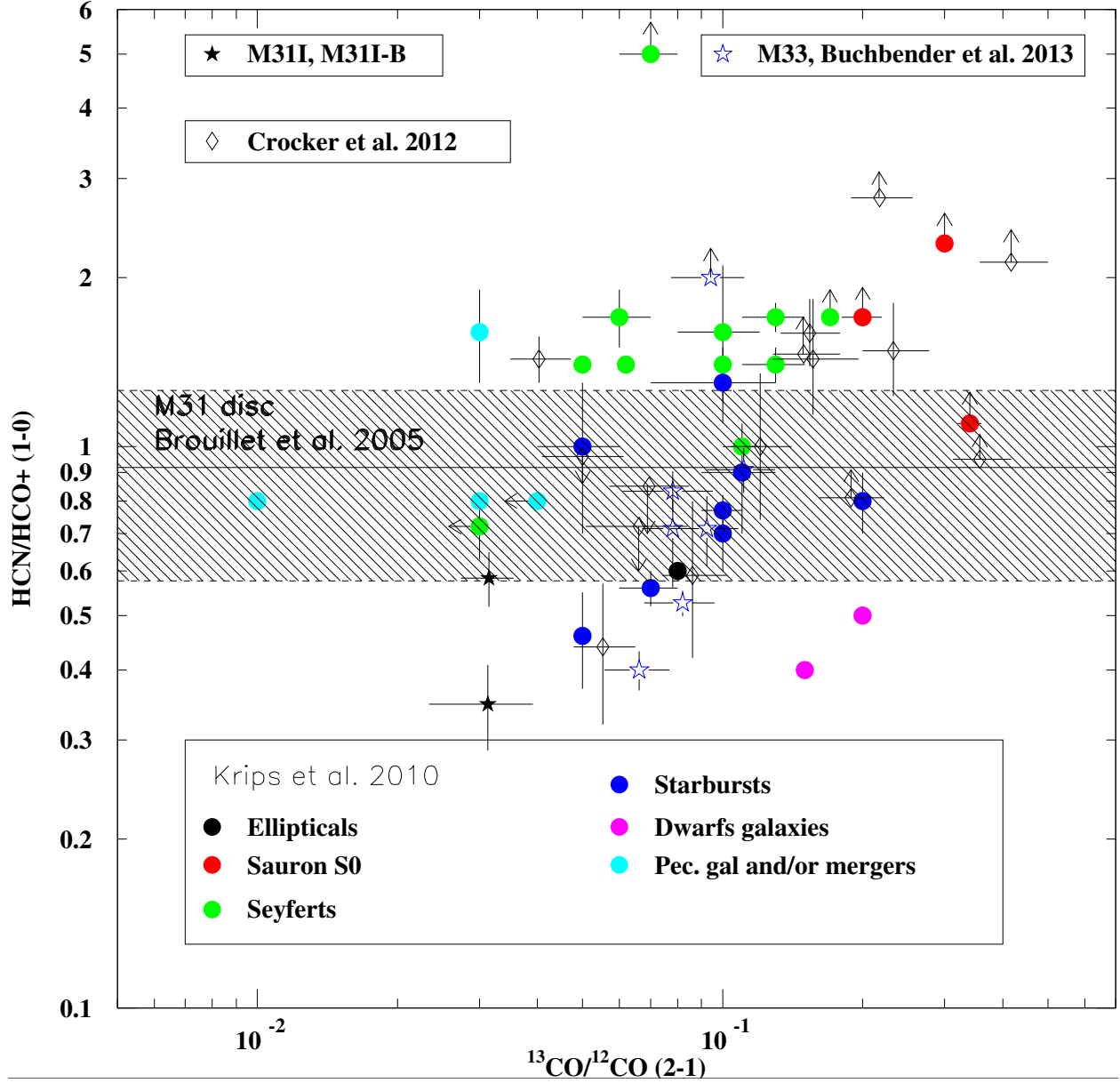


**Fig. 10.** Comparison with other catalogues (1). HCN/HCO+(1-0) line ratio versus  $^{13}\text{CO}/^{12}\text{CO}(2-1)$  line ratio. The two detections presented in this paper (M31I and M31I-B) are superimposed on previous measurements, namely: a compilation of various types of galaxies from Krips et al. (2010), early-type galaxies from Crocker et al. (2012) and M33's giant molecular clouds from Buchbender et al. (2013). The hatched area corresponds to the mean HCN/HCO+(1-0) line ratio obtained by Brouillet et al. (2005) in M31's disc. Surprisingly, our detections lie in "the starburst region".

If the molecular lines are close to thermal equilibrium around 20 K, the beam filling factor is below one percent. This order of magnitude is coherent with different qualitative arguments. The beam size is 44 pc for  $^{12}\text{CO}$ , while typical interstellar filaments have a size of 0.1 pc (André et al. 2014). We are detecting gas complexes, which are probably more extended and patchy according to the optical image. The large velocity dispersions also suggest that we are integrating gas along a large depth. Last, if one consider a standard gas-to-dust rela-

tion  $N_H = 0.94 \times 10^{21} \times A_V \text{ cm}^{-2}$  (Bohlin et al. 1978), we estimate  $A_V = 2.5$  and 1.4 for M31-I(2) and M31-IB(1) (with no beam-filling factor corrections), while lower limits on extinction estimated on the optical images are of the order of  $A_B = 0.2$  (Melchior & Combes 2011). This order of magnitude of the beam filling factor is compatible with values previously discussed in the literature, e.g. Carlstrom (1988) estimated a volume filling factor smaller than  $10^{-3}$  in M82, while Berkhuijsen & Fletcher

**Table 7.** Considering that the  $^{12}\text{CO}(2-1)$  line is optically thick, we estimate the beam filling factor  $\eta_{bf}(T_{ex})$  for different excitation temperatures, namely 25, 20, 15, 10, 5 K. The next four columns provide the optical depths for  $^{13}\text{CO}(2-1)$ ,  $\text{C}^{18}\text{O}(2-1)$ ,  $\text{HCO}^+(1-0)$  and  $\text{HCN}(1-0)$  assuming an excitation temperature of 20 K and a beam filling factor equal to the one derived from  $^{12}\text{CO}$ :  $\eta_{bf}(20\text{ K})$ . The next two columns provides the  $^{12}\text{CO}(2-1)$  column densities computed for two standard  $^{12}\text{CO}/^{13}\text{CO}$  line ratios for the molecular ring (MR) and the Galactic centre (GC) from Wilson & Rood (1994).

Positions	$\eta_{bf}(25\text{ K})$	$\eta_{bf}(20\text{ K})$	$\eta_{bf}(15\text{ K})$	$\eta_{bf}(10\text{ K})$	$\eta_{bf}(5\text{ K})$	$\tau_{^{13}\text{CO}}$	$\tau_{\text{C}^{18}\text{O}}$	$\tau_{\text{HCO}^+}$	$\tau_{\text{HCN}}$	$\tau_{^{12}\text{CO}}^{\text{MR}}$	$\tau_{^{12}\text{CO}}^{\text{GC}}$
I(1)	$2.1 \times 10^{-2}$	<b><math>2.9 \times 10^{-2}</math></b>	$4.2 \times 10^{-2}$	$8.0 \times 10^{-2}$	$3.6 \times 10^{-1}$	0.58				30.30	11.44
I(2)	$7.4 \times 10^{-3}$	<b><math>9.9 \times 10^{-3}</math></b>	$1.5 \times 10^{-2}$	$2.8 \times 10^{-2}$	$1.2 \times 10^{-1}$	0.03		0.02	0.02	1.68	0.63
I(3)	$3.9 \times 10^{-3}$	<b><math>5.2 \times 10^{-3}</math></b>	$7.7 \times 10^{-3}$	$1.5 \times 10^{-2}$	$6.6 \times 10^{-2}$	0.07	0.06			3.44	1.30
I-B(1)	$7.0 \times 10^{-3}$	<b><math>9.3 \times 10^{-3}</math></b>	$1.4 \times 10^{-2}$	$2.6 \times 10^{-2}$	$1.2 \times 10^{-1}$	0.10		0.03	0.04	5.18	1.95
I-B(2)	$1.3 \times 10^{-3}$	<b><math>1.7 \times 10^{-3}</math></b>	$2.5 \times 10^{-3}$	$4.7 \times 10^{-3}$	$2.1 \times 10^{-2}$	0.13				6.69	2.52
2d-a(1)	$5.1 \times 10^{-3}$	<b><math>6.7 \times 10^{-3}</math></b>	$1.0 \times 10^{-2}$	$1.9 \times 10^{-2}$	$8.5 \times 10^{-2}$	0.06				3.13	1.18
2d-a(2)	$5.3 \times 10^{-3}$	<b><math>7.1 \times 10^{-3}</math></b>	$1.1 \times 10^{-2}$	$2.0 \times 10^{-2}$	$9.0 \times 10^{-2}$	0.05				2.50	0.94
2d-b(1)	$8.9 \times 10^{-3}$	<b><math>1.2 \times 10^{-2}</math></b>	$1.8 \times 10^{-2}$	$3.3 \times 10^{-2}$	$1.5 \times 10^{-1}$	0.02				0.96	0.36
2d-b(2)	$2.2 \times 10^{-3}$	<b><math>3.0 \times 10^{-3}</math></b>	$4.4 \times 10^{-3}$	$8.3 \times 10^{-3}$	$3.8 \times 10^{-2}$	0.06				3.31	1.25
2d-b(3)	$1.9 \times 10^{-3}$	<b><math>2.6 \times 10^{-3}</math></b>	$3.8 \times 10^{-3}$	$7.2 \times 10^{-3}$	$3.2 \times 10^{-2}$	0.14				7.07	2.67
2c-a(1)	$3.1 \times 10^{-3}$	<b><math>4.1 \times 10^{-3}</math></b>	$6.1 \times 10^{-3}$	$1.2 \times 10^{-2}$	$5.2 \times 10^{-2}$						
2c-a(2)	$2.7 \times 10^{-3}$	<b><math>3.7 \times 10^{-3}</math></b>	$5.4 \times 10^{-3}$	$1.0 \times 10^{-2}$	$4.6 \times 10^{-2}$						
2c-a(3)	$5.0 \times 10^{-3}$	<b><math>6.6 \times 10^{-3}</math></b>	$9.8 \times 10^{-3}$	$1.9 \times 10^{-2}$	$8.4 \times 10^{-2}$						

(2015) estimate a filling factor of order 4% in M31 and M51.

In the following, we consider that  $^{12}\text{CO}(2-1)$  is optically thick to determine the beam filling factors at thermal equilibrium, as provided in Table 7. For a given excitation temperature, we can derive the optical depth corresponding to each optically thin line:

$$\tau_{mol} = -\ln \left( 1 - \frac{T_{peak}}{\eta_{bf}} \frac{1}{f(T_{ex}) - f(T_{bg})} \right) \quad (5)$$

We can then compute the column density associated to each molecular line assuming an excitation temperature  $T_{ex}$ :

$$N_{mol} = \frac{8\pi k}{hc^3} \frac{Q(T)}{g} e^{E_{up}/T_{ex}} \frac{\tau}{1 - e^{-\tau}} \frac{\nu^2 I_{CO}}{\eta_{bf}} \quad (6)$$

where  $g$  is the level degeneracy  $g = 5$  for  $\text{CO}(2-1)$  molecules and  $g = 3$  for  $\text{HCN}(1-0)$  and  $\text{HCO}^+(1-0)$ ,  $Q(T)$  is the rotational partition function and  $E_{up}$  is the energy level provided in Table 3. We also consider the beam filling factors defined in Table 7. The factor  $\frac{\tau}{1 - e^{-\tau}}$  enables to account for non-optically thin conditions (e.g. Mangum & Shirley 2015). However, in practice, we have to assume an unknown abundance, which limits the use of corrected column density in this analysis.

In Sect. 4.4, we discuss abundances estimated assuming local thermal equilibrium (LTE) conditions. In Sect. 4.5, we explore with RADEX simulations (van der Tak et al. 2007) how to derive molecular hydrogen densities allowing lower excitation temperatures.

#### 4.4. Local Thermal Equilibrium conditions

We consider here that the different detected lines correspond to some gas in LTE with an excitation temperature of 20 K.

##### 4.4.1. Optical depth

With these assumptions, we have derived optical depths for  $^{13}\text{CO}(2-1)$ ,  $\text{C}^{18}\text{O}(2-1)$ ,  $\text{HCO}^+(1-0)$  and  $\text{HCN}(1-0)$  with the filling factor  $\eta_{bf}(20\text{ K})$ . These lines are optically thin, as displayed in Table 7.

If we consider standard  $^{12}\text{CO}/^{13}\text{CO}$  line ratios from Wilson & Rood (1994) of 53 for the molecular ring (resp. 20 for the Galactic centre) and the  $^{13}\text{CO}$  optical depths provided in Table 7, we estimate an average optical depth for  $^{12}\text{CO}$  of 6.5 (resp. 2.5). The  $^{12}\text{CO}(2-1)$  transition is indeed optically thick. These different optical depths discussed above are provided for each line of sight in Table 7.

##### 4.4.2. Column densities

In the middle panel of Table 4, we provide column densities of our main detections ( $^{13}\text{CO}$ ,  $\text{C}^{18}\text{O}$ ,  $\text{HCN}$ ,  $\text{HCO}^+$ ) and some upper limits, with optically thin gas ( $\tau \ll 1$ ) in LTE.

In the right panel of Table 4, we also provide the column density of molecular hydrogen derived empirically from the  $^{12}\text{CO}$  line intensity with a  $X_{\text{CO}}$  factor as discussed in Sect. 3.

All the column densities account for the beam filling factor  $\eta_{bf}$ .

##### 4.4.3. Abundance ratios

In Table 8, we tentatively compute the abundances (i.e. the ratio of the column density of the molecule with respect to the column density of molecular hydrogen) for M31-I(3) and the stacking of the  $^{13}\text{CO}(2-1)$  detections, where  $^{13}\text{CO}(2-1)$  and  $\text{C}^{18}\text{O}(2-1)$  have been detected, and M31-I(2) where  $\text{HCN}$  and  $\text{HCO}^+$  have been detected.

**Table 8.** Abundance ratio. For each molecule, we provide the expected abundances assuming LTE and optically thin conditions, to compare them with Galactic values. We provide abundances and abundance ratios for 2 positions M31-I(3) and M31-I(2) and the stacking detection (columns 2-5), then compare these values with those expected for the Galactic interstellar medium (at 4 kpc derived from Bergin et al. (1995) and Wilson & Rood (1994)) (columns 6-9).

Transition (2-1)	Measured values (LTE)				Galactic values			
	I(3)		Stacking		$X^{GISM}$		$^{13}\text{CO}/\text{C}^{18}\text{O}$	
	$X^{Obs}$	$^{13}\text{CO}/\text{C}^{18}\text{O}$	$X^{Obs}$	$^{13}\text{CO}/\text{C}^{18}\text{O}$	(MR)	(GC)	(MR)	(GC)
$^{13}\text{CO}$	$1.3 \times 10^{-7}$	1	$8.1 \times 10^{-7}$	1	$5.3 \times 10^{-7}$	$1.4 \times 10^{-6}$	1	1
$\text{C}^{18}\text{O}$	$9.8 \times 10^{-8}$	1.3	$8.2 \times 10^{-7}$	0.99	$8.6 \times 10^{-8}$	$1.1 \times 10^{-7}$	6.2	12.7
Transition (1-0)	I(2) - Measured values (LTE)				Galactic values			
	$X^{Obs}$	$\text{HCN}/\text{HCO}+$	$\text{HCO}+/\text{HCN}$		$X^{GISM}$	$\text{HCN}/\text{HCO}+$	$\text{HCO}+/\text{HCN}$	
HCN	$2.6 \pm 1.0 \cdot 10^{-10}$	1	0.7		$1.9 \times 10^{-9}$	1	0.25	
HCO+	$1.81 \pm 0.46 \cdot 10^{-10}$	1.4	1		$4.7 \times 10^{-10}$	4.0	1	

In order to perform ratio of lines measured with similar HPBW resolutions, we use  $^{12}\text{CO}(2-1)$  to derive the molecular hydrogen column density for the  $^{13}\text{CO}$  and  $\text{C}^{18}\text{O}$  measurements and  $^{12}\text{CO}(1-0)$  (available for M31-I) for HCN and HCO+ abundances, as presented in Table 4 and described in Sect. 3. We can note that the molecular hydrogen column density exhibits variations with different resolutions ( $11''$  and  $21''$ ) of a factor up to 3. We also provide for comparison the abundance values for the Galaxy computed in the molecular ring (MR) at 4 kpc from the Galactic centre and in the Galactic centre (GC) by Bergin et al. (1995) and Wilson & Rood (1994).

The abundances are affected by the uncertainties on the molecular hydrogen column densities computed empirically with the  $X_{\text{CO}}$  factor and by the uncertainties on the excitation temperatures. For the CO transitions, we can expect that variations of the excitation temperatures are a secondary effect, and we can thus rely on abundance ratios for optically thin transitions. The detected  $^{13}\text{CO}/\text{C}^{18}\text{O}$  abundance ratios are very different from the Galactic values. There is a discrepancy of a factor 6 with the molecular ring, and a factor 13 with respect to the Galactic centre where gas has been processed regularly. Obviously the gas is not in the same state as these obvious regions in the Galaxy. Considering the  $\text{C}^{18}\text{O}$  abundances in M31-I(3), it is relatively close to the Galactic centre value, while the discrepancy affects the  $^{13}\text{CO}$ . For the stacking, the  $\text{C}^{18}\text{O}$  abundance is stronger than the Galactic value, but the uncertainties have probably been introduced in the  $^{12}\text{CO}$  averaging process. If the  $\text{C}^{18}\text{O}$  abundance is scaled to the Galactic value, the  $^{13}\text{CO}$  is deficient.

The HCN and HCO+ abundances differ from the Galactic values, as well as the abundance ratio. These discrepancies could be due to different excitation temperatures. The lower limit on the HCN/HNC abundance ratio derived here are 1.8 and 1.4, which is sufficient to put some constraints on the kinetic temperature (e.g. Schilke et al. 1992; Hirota et al. 1998). This corresponds to kinetic temperatures larger than 28K. This is compatible with the

results of Viaene et al. (2014) based on the analysis of infrared data. Similarly, we get HCO+/HOC+ abundance ratios larger 4.1 and 5, but this is not restrictive enough as previous detections are in the range 50-12500 (Savage & Ziurys 2004).

In the next Section, we explore with non-LTE simulations how different excitation temperatures could affect the different parameters and help to get a coherent set of parameters.

#### 4.5. RADEX simulations

In order to check the consistency of our parameters, we have run some RADEX simulations (van der Tak et al. 2007) for several molecules. The idea is to relax the LTE conditions and get an estimate of the excitation temperature and the molecular hydrogen density of the detected gas.

In Figure 11, we display the results of the simulations run for HCN and superimpose the various parameters discussed in the previous section, namely the optical depth, the molecule column densities per unit velocity derived from our observations and from the standard abundances. These results support the view that this gas is subthermally excited at 10 K with a density smaller than the critical density. This is also consistent with the HCN(1-0) transition being optically thin. We have detected two dense clumps with a molecular hydrogen density  $n_{\text{H}_2} = 5.6 \times 10^5 \text{ cm}^{-3}$  in the North-West side of the inner ring. Our abundances are more than a factor of 10 weaker than the column densities derived from the standard abundances estimated by Bergin et al. (1995) in the molecular ring (MR), and the discrepancy would be even larger if one considers the Galactic centre conditions.

We performed similar simulations for HCO+(1-0), as displayed in Figure A.4. We also find subthermal conditions with a molecular hydrogen density smaller than the critical density and an excitation temperature of 8 K. The abundances are also smaller (factor 3.6) than the column densities derived from the standard MR abundances

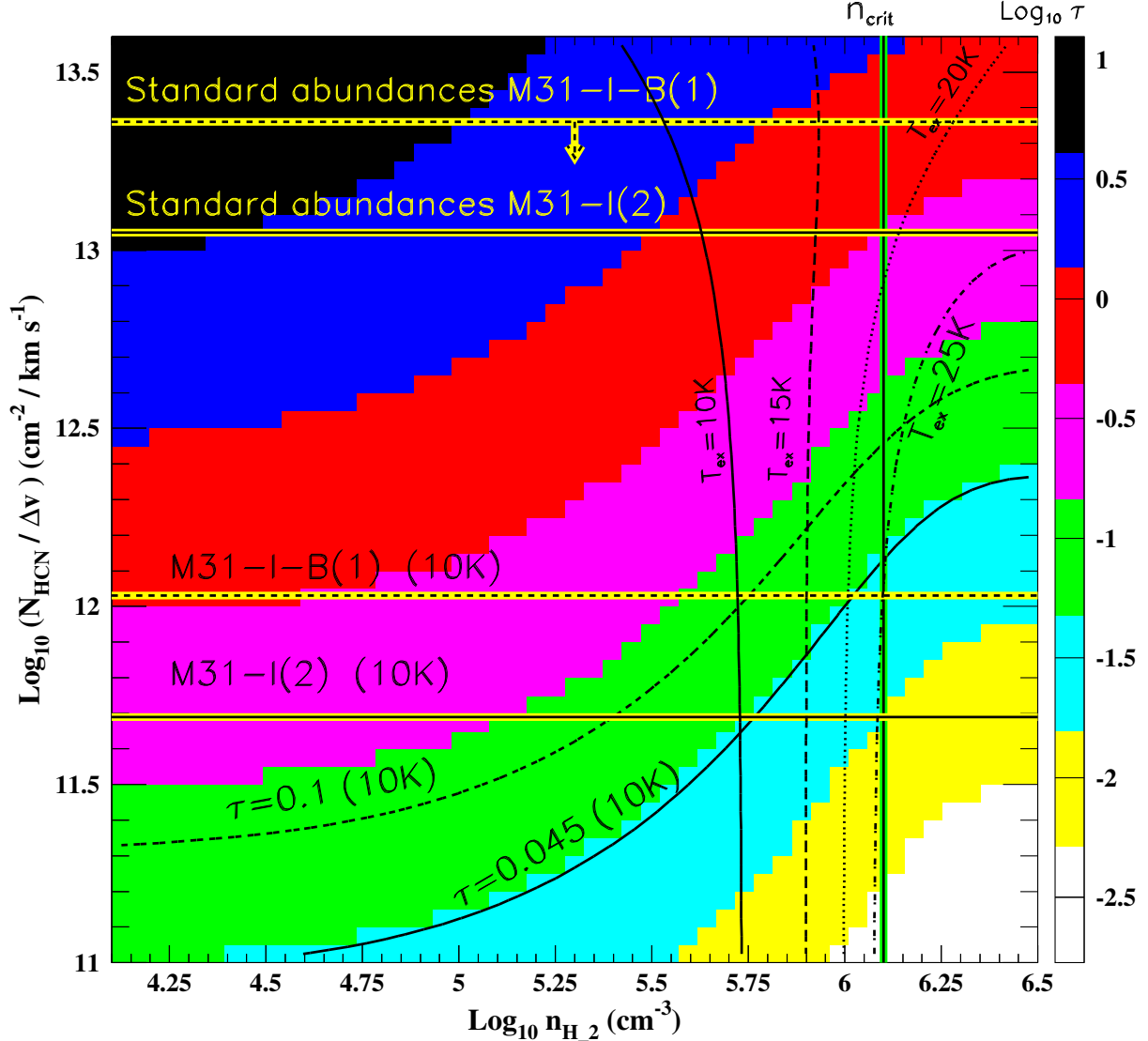


**Fig. 11.** Main physical parameters corresponding to the HCN gas observed in M31-I(2) and M31-I-B(1). The optical depths are displayed as function of the HCN column density (per  $\text{km s}^{-1}$ ) and the molecular hydrogen density  $n_{\text{H}_2}$ . The corresponding contours for these two clumps are displayed in dashed line (for M31-I-B(1)) and in full line (for M31-I(2)). The vertical (green) line indicates the critical density computed for a collisional temperature of 20 K (see Table 3). The lower horizontal full (resp. dashed) line displays the column density measured for M31-I(2) (resp. M31-I-B(1)) at 10 K. The upper horizontal lines correspond to the column densities computed with standard abundances (Bergin et al. 1995) and the corresponding molecular hydrogen column densities. For M31-I-B(1), we derive an upper limit as the molecular hydrogen column density is only available for a smaller beam (see Table 4) and we expect some dilution of the signal. The contour levels correspond to excitation temperatures of 8 K (full line), 10 K (dashed line), 15 K (dotted line) and 20 K (dash-dot line).

(Bergin et al. 1995). The gas associated to the  $\text{HCO}^+(1-0)$  detection has a density of  $6.3 \times 10^4 \text{ cm}^{-3}$ .

The same procedure has been applied to M31-I(3) where  $^{13}\text{CO}$  and  $\text{C}^{18}\text{O}$  have been detected, as displayed in Figure 12. On the one hand, the best excitation temperature is consistent with 17.5 K but given the error bars we cannot exclude 20 K. On the other hand, the simulations support a molecular hydrogen density larger than the crit-

ical density. These lines are close to LTE conditions and trace clumps with a density larger than  $2.5 \times 10^4 \text{ cm}^{-3}$ . The  $^{13}\text{CO}$  measured abundance is smaller than the standard abundances by a factor 4, while the  $\text{C}^{18}\text{O}$  measured abundance is compatible within the error bars with the standard abundances estimated in the molecular ring.

The abundances we have derived are systematically smaller than the standard abundances (Bergin et al. 1995)



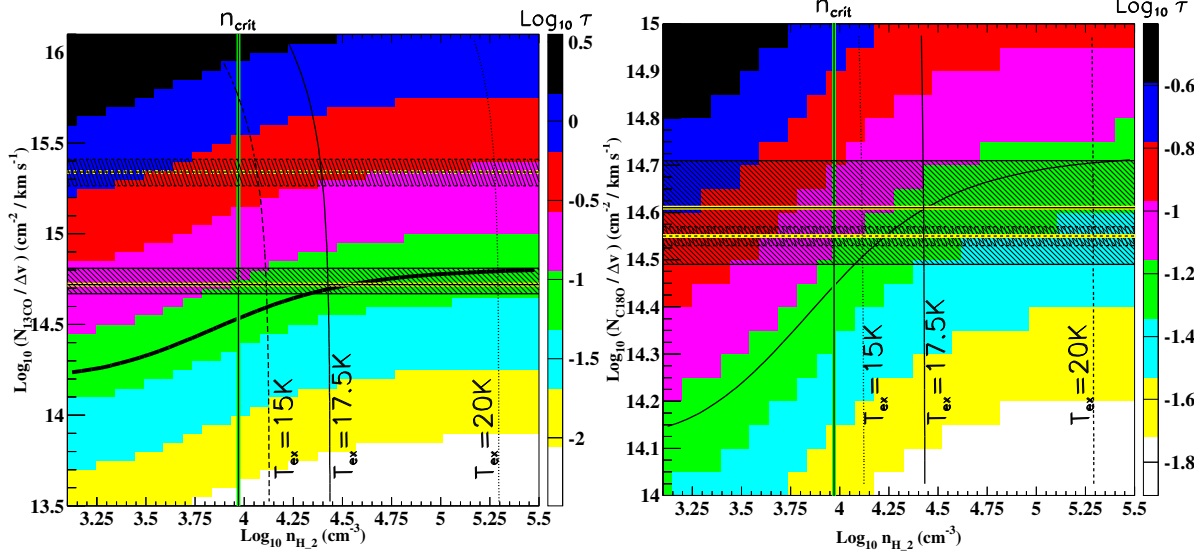


**Fig. 12.** Main physical parameters corresponding to the  $^{13}\text{CO}(2-1)$  gas (left panel) and the  $\text{C}^{18}\text{O}(2-1)$  gas (right panel) detected in M31-I(3). The optical depths are displayed as function of the  $^{13}\text{CO}(2-1)$  column density (per  $\text{km s}^{-1}$ ) and the molecular hydrogen density  $n_{\text{H}_2}$ . The vertical green lines indicate the critical densities computed for a collisional temperature of 20 K (see Table 3). The horizontal thick full yellow-black line (resp. thin black lines) display the  $^{13}\text{CO}(2-1)$  (left panel) and the  $\text{C}^{18}\text{O}(2-1)$  averaged column densities (per unit velocity) (resp.  $1\sigma$  standard deviation): this area corresponding to the M31-I(3) detection has been hatched. The horizontal thick dashed yellow-black line (resp. thin black lines) corresponds to the column densities (resp.  $1\sigma$  standard deviation) computed with standard abundances (Bergin et al. 1995) and the corresponding molecular hydrogen densities. The full-line (resp. dashed and dotted) contour level corresponds to an excitation temperature of 17.5 K (resp. 15 K and 20 K). The mean optical depth is displayed as a thick line contour level. The combination of the measured optical depth and abundance favours an excitation temperature of 17.5 K and a molecular hydrogen density larger than the critical one. However, an excitation temperature of 20 K and a larger density cannot be excluded given the uncertainties. The  $\text{C}^{18}\text{O}$  (resp.  $^{13}\text{CO}$ ) detected abundance is compatible with (resp. smaller than) the column density derived from the standard abundances (Bergin et al. 1995) and the molecular hydrogen column densities derived from  $^{12}\text{CO}$  detection.

for the molecular ring, but for  $\text{C}^{18}\text{O}$ . This is consistent with our previous discussion that  $^{12}\text{CO}$  is optically thick and  $^{13}\text{CO}$  depleted, with LTE and optically thin conditions for  $^{13}\text{CO}$  and  $\text{C}^{18}\text{O}$ . HCN and  $\text{HCO}^+$  abundances are consistent with subthermal excitation conditions with excitation temperatures of 10 K and 8 K and are smaller than the standard abundances. One can also note as displayed in Figure A.2,  $\text{HCO}^+/\text{HCN}$  line ratio is larger in the clouds studied here than in the clouds studied in M31's disc by Brouillet et al. (2005).

## 5. Heating sources

### 5.1. X-ray flux

Following Bogdán & Gilfanov (2008), we know that the diffuse gas detected in this area within  $150\text{--}200''$  from the centre is weak. The detected flux lies in the range  $1.6 - 9 \times 10^{-18} \text{ erg s}^{-1} \text{ cm}^{-2} \text{ arcsec}^{-2}$  considering a size of molecular cloud of 1 pc and a distance of M31 of 780 kpc, we can estimate a rough X-ray incident radiation intensity of  $6\text{--}34 \times 10^{-7} \text{ erg s}^{-1} \text{ cm}^{-2}$ . This is at least five orders of magnitude weaker than the radiation field considered by Meijerink et al. (2007) for XDR modelling.

There is only one ROSAT (Second ROSAT PSPC catalogue) source within  $12''$  (resp.  $22''$ ) from M31I (resp. M31I-B) with a  $14\text{ arcsec}$  positional error, with a flux of  $10^{-12} \text{ erg s}^{-1} \text{ cm}^{-2} \text{ arcsec}^{-2}$ . There is no Chandra or XMM source in this area. In this inner region, the contribution of the central black hole could be significant. However, Li et al. (2011) have measured Chandra X-Ray Observatory a burst of activity in January 2006 at a level of  $4.3 \times 10^{37} \text{ erg s}^{-1}$  and a quiescent level of  $4.8 \times 10^{36} \text{ erg s}^{-1}$ . At the distance of M31I and M31I-B (supposed in the sky plane), this would contribute to the X-ray incident radiation intensity at a level of  $7.3 \times 10^{-8} \text{ erg s}^{-1} \text{ cm}^{-2}$  (resp.  $6.6 \times 10^{-7} \text{ erg s}^{-1} \text{ cm}^{-2}$ ) in the quiescent state (resp. during the outburst).

We can thus exclude that the excitation mechanism of the gas is due to X-ray radiation.

### 5.2. Interstellar radiation field

There are two GALEX (Release 6) sources with a detected FUV flux of  $6 \pm 2$  and  $7.5 \pm 1.5 \mu\text{Jy}$ , within  $12''$  (resp.  $18''$ ) of M31I (resp. M31I-B). This would contribute to the radiation field at a negligible level of  $6 \times 10^{-3} G_0$  at

a distance larger than 45 pc. If we consider the FUV GALEX flux at the position of M31I, we estimate that its contribution to radiation field should be larger than  $0.06G_0$  (GALEX does not sample the 912-1344Å interval). This is again very weak. The heating is mainly due to the old stellar population as discussed by Draine et al. (2014) and Viaene et al. (2014). The Mathis et al. (1983) based  $U$  computed by Draine et al. (2014) are provided in Table 1. The area around M31I and M31I-B have  $U = 1.5$ , while the other 3 positions have  $U$  in the range 1.8-2.7. This corresponds according to Draine et al. (2014) to an average dust temperature of 20 K. If we assume a thermalised medium, the kinetic temperature should be similar.

If there is some star formation activity, as the gas is very clumpy as found with the analysis of the molecular gas detection, the local radiation field could be hidden in the clump. This could explain why there is no obvious star forming region in the UV.

## 6. Conclusion

We have detected  $^{12}\text{CO}(2-1)$  and  $^{13}\text{CO}(2-1)$  lines with multiple velocity components along the minor axis of M31 on both sides of the inner 1-kpc ring. Dense gas  $\text{C}^{18}\text{O}(2-1)$ ,  $\text{HCN}(1-0)$  and  $\text{HCO}^+(1-0)$  have been detected in the North-West side in the blue-shifted component and  $\text{C}^{18}\text{O}$  has also been detected at the systemic velocity. The stellar heating in this area has been measured smaller in the North-West side by Draine et al. (2014) and Viaene et al. (2014), which could explain why dense gas has only been detected on this side. A careful analysis has shown that  $^{12}\text{CO}$  is optically thick while the other CO lines are optically thin and close to LTE at an excitation temperature of 17.5-20 K. The gas is very clumpy and the averaged beam filling factor is 0.8%. The average column density of molecular hydrogen is  $16 \times 10^{22} \text{ cm}^{-2}$ . The derived abundances are all smaller than the standard abundances, but for  $\text{C}^{18}\text{O}$ . The comparison of the derived abundances with RADEX simulations shows that the HCN and  $\text{HCO}^+$  gas correspond to dense clumps with molecular hydrogen density of the range  $6 \times 10^4 - 6 \times 10^5 \text{ cm}^{-3}$  and an excitation temperature of 8-10 K. The  $\text{HCO}^+/\text{HCN}$  line ratio is systematically larger than for clouds detected in M31's disc (Brouillet et al. 2005), while the derived abundances are smaller than the Galactic ones (Bergin et al. 1995), with a larger discrepancy for HCN. No bright objects, typical of star formation regions, are identified in X-ray or UV, while the bulge stellar population is sufficient to heat the gas and reproduce the infrared maps. These detections are all weak and close to the detection limits.  $\text{C}^{18}\text{O}$  has been detected in a single point at the systemic velocity. Stacking of all  $^{13}\text{CO}$  detections has revealed the underlying presence of  $\text{C}^{18}\text{O}$  gas in the blueshifted component. Both the single point and the stacking detections have an overall intensity comparable to  $^{13}\text{CO}$ . As we expect  $\text{C}^{18}\text{O}$  to be 6 times less abundant than  $^{13}\text{CO}$  and the measured abundance of  $\text{C}^{18}\text{O}$  is compatible with the standard abundance,  $^{13}\text{CO}$

should be depleted. A coherent explanation is that  $^{13}\text{C}$  has been depleted during a starburst. This is compatible with the Block et al. (2006) scenario suggesting a frontal collision with a nearby companion galaxy such as M32. This collision explains the ring and has triggered a starburst at the epoch of the collision. This is also in agreement with the central starburst which occurred next to the black hole 200 Myr ago (Lauer et al. 2012).

*Acknowledgements.* We thank the IRAM staff in Granada for their help during the observations. We are most grateful to S. Vianey for providing us with the maps produced in the Vianey et al. 2014 paper. We have used GALEX and ROSAT archive data in Section 5.

## References

- André, P., Di Francesco, J., Ward-Thompson, D., et al. 2014, *Protostars and Planets VI*, 27
- Bacon, R., Emsellem, E., Combes, F., et al. 2001, *A&A*, 371, 409
- Bender, R., Kormendy, J., Bower, G., et al. 2005, *ApJ*, 631, 280
- Bergin, E. A., Langer, W. D., & Goldsmith, P. F. 1995, *ApJ*, 441, 222
- Berkhuijsen, E. M., & Fletcher, A. 2015, *arXiv:1501.07769*
- Block, D. L., Bournaud, F., Combes, F., et al. 2006, *Nature*, 443, 832
- Bogdán, Á., & Gilfanov, M. 2008, *MNRAS*, 388, 56
- Bohlin, R. C., Savage, B. D., & Drake, J. F. 1978, *ApJ*, 224, 132
- Brouillet, N., Muller, S., Herpin, F., Braine, J., & Jacq, T. 2005, *A&A*, 429, 153
- Buchbender, C., Kramer, C., Gonzalez-Garcia, M., et al. 2013, *A&A*, 549, A17
- Carlstrom, J. E. 1988, *Molecular Clouds, Milky-Way and External Galaxies*, 315, 405
- Casoli, F., Dupraz, C., Combes, F., & Kazes, I. 1991, *A&A*, 251, 1
- Crane, P. C., Dickel, J. R., & Cowan, J. J. 1992, *ApJ*, 390, L9
- Crocker, A., Krips, M., Bureau, M., et al. 2012, *MNRAS*, 421, 1298
- Dame, T. M., Hartmann, D., & Thaddeus, P. 2001, *ApJ*, 547, 792
- Davis, MNRAS, accepted
- Draine, B. T., Aniano, G., Krause, O., et al. 2014, *ApJ*, 780, 172
- Draine, B. T., & Li, A. 2007, *ApJ*, 657, 810
- Ford, G. P., Gear, W. K., Smith, M. W. L., et al. 2013, *ApJ*, 769, 55
- Garcia, M. R., Hextall, R., Baganoff, F. K., et al. 2010, *ApJ*, 710, 755
- Groves, B., Krause, O., Sandstrom, K., et al. 2012, *MNRAS*, 426, 892
- Hirota, T., Yamamoto, S., Mikami, H., & Ohishi, M. 1998, *ApJ*, 503, 717
- Krips, M., Crocker, A. F., Bureau, M., Combes, F., & Young, L. M. 2010, *MNRAS*, 407, 2261
- Lauer, T. R., Bender, R., Kormendy, J., Rosenfield, P., & Green, R. F. 2012, *ApJ*, 745, 121
- Li, Z., Garcia, M. R., Forman, W. R., et al. 2011, *ApJ*, 728, L10
- Li, F.-C., Wu, Y.-W., & Xu, Y. 2014, *arXiv:1411.4349*
- Liu, X.-L., Wang, J.-J., & Xu, J.-L. 2014, *MNRAS*, 443, 2264
- McConnachie, A. W., Irwin, M. J., Ibata, R. A., et al. 2009, *Nature*, 461, 66
- Mangum, J. G., & Shirley, Y. L. 2015, *arXiv:1501.01703*
- Mathis, J. S., Mezger, P. G., & Panagia, N. 1983, *A&A*, 128, 212
- Matsushita, S., Kawabe, R., Kohno, K., Tosaki, T., & Vila-Vilaró, B. 2010, *PASJ*, 62, 409
- Mauersberger, R., Henkel, C., Weiß, A., Peck, A. B., & Hagiwara, Y. 2003, *A&A*, 403, 561
- Meijerink, R., Spaans, M., & Israel, F. P. 2007, *A&A*, 461, 793
- Melchior, A.-L., Viallefond, F., Guélin, M., & Neininger, N. 2000, *MNRAS*, 312, L29
- Melchior, A.-L., & Combes, F. 2011, *A&A*, 536, A52
- Melchior, A.-L., & Combes, F. 2013, *A&A*, 549, A27
- Nishimura, A., Tokuda, K., Kimura, K., et al. 2015, *ApJS*, 216, 18
- Savage, C., & Ziurys, L. M. 2004, *ApJ*, 616, 966
- Schilke, P., Walmsley, C. M., Pineau Des Forets, G., et al. 1992, *A&A*, 256, 595
- Schinnerer, E., Weiß, A., Aalto, S., & Scoville, N. Z. 2010, *ApJ*, 719, 1588

- Schöier, F. L., van der Tak, F. F. S., van Dishoeck, E. F., & Black, J. H. 2005, *A&A*, 432, 369
- Smith, M. W. L., Eales, S. A., Gomez, H. L., et al. 2012, *ApJ*, 756, 40
- Strong, A. W., Bloemen, J. B. G. M., Dame, T. M., et al. 1988, *A&A*, 207, 1
- Tan, Q.-H., Gao, Y., Zhang, Z.-Y., & Xia, X.-Y. 2011, *Research in Astronomy and Astrophysics*, 11, 787
- van der Tak, F. F. S., Black, J. H., Schöier, F. L., Jansen, D. J., & van Dishoeck, E. F. 2007, *A&A*, 468, 627
- Viaene, S., Fritz, J., Baes, M., et al. 2014, *A&A*, 567, A71
- Wilson, T. L., & Rood, R. 1994, *ARA&A*, 32, 191

## **Appendix A: Additional Figures**

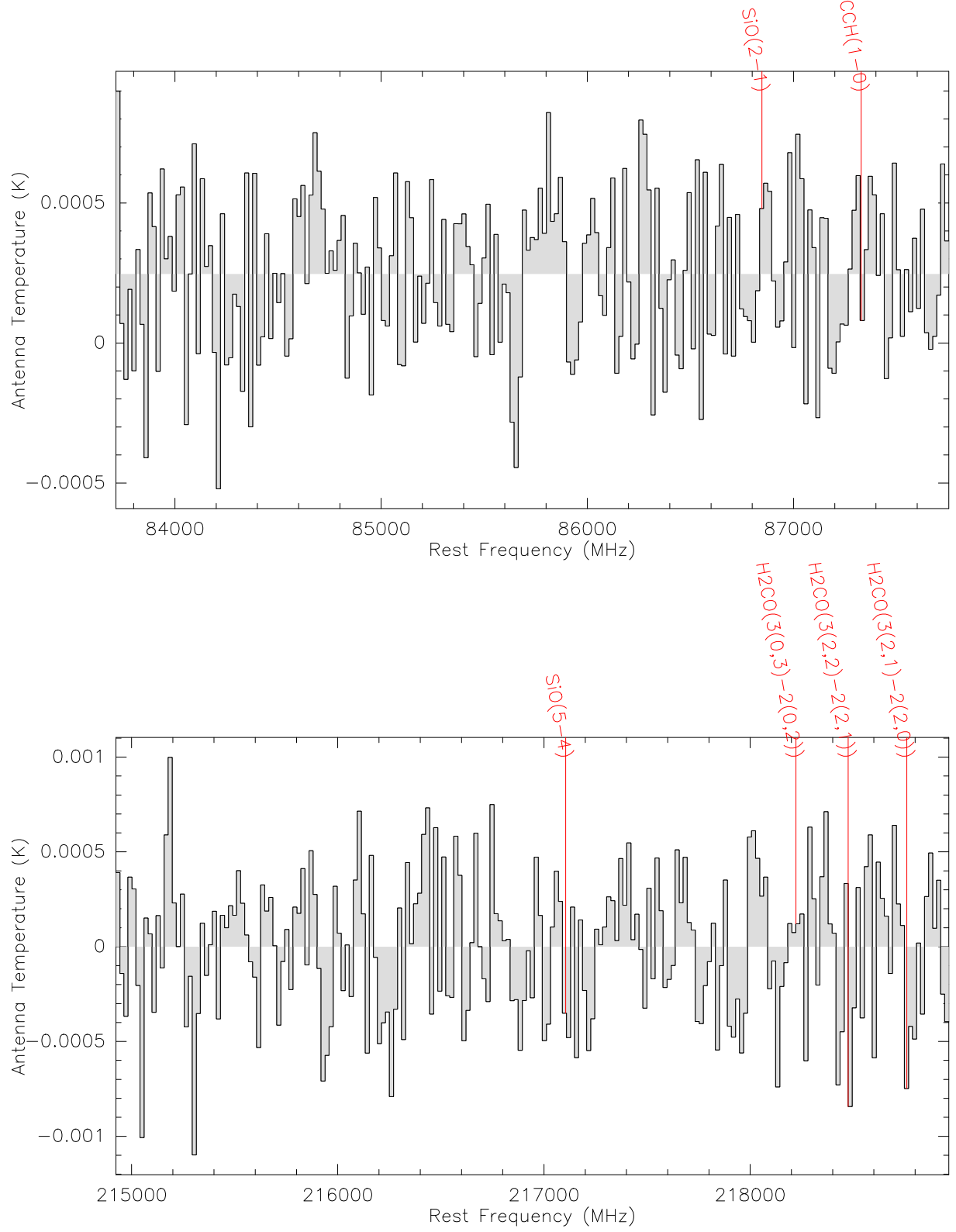


**Fig. A.1.** Averaging of the observations performed in the EMIR lower outer (LO) bands. The different lines present in the bandwidth are plotted in the restframe frequency. No signal is detected. This has been used to derived detection limit in Table 4.

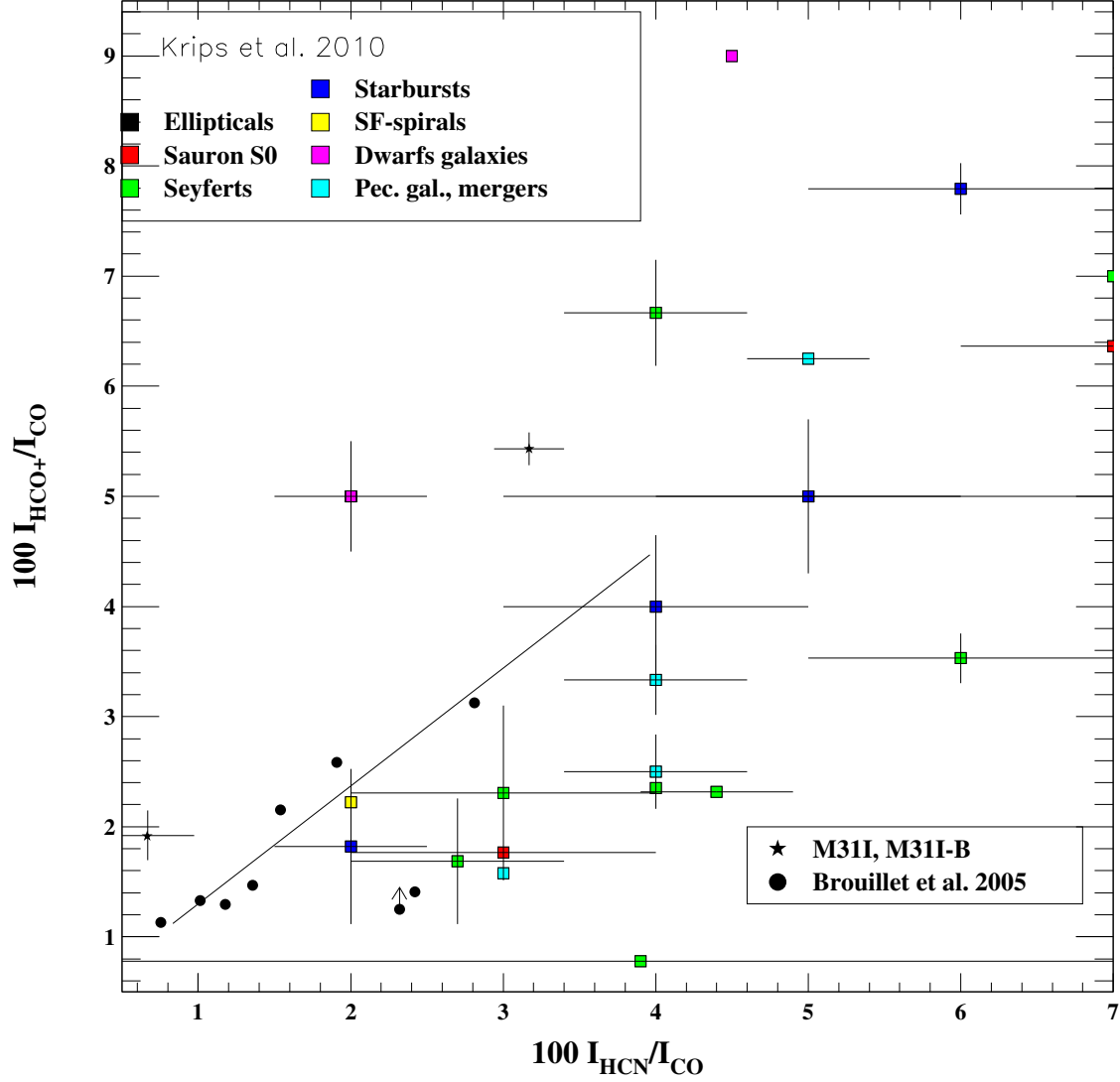


**Fig. A.2.** Comparison with other catalogues (2).  $\text{HCO}^+/\text{CO}(1-0)$  line ratio versus  $\text{HCN}/\text{CO}$  line ratio. The two detections presented in this paper (M31I and M31I-B) are superimposed on previous measurements, namely: detection of across M31's main disc by Brouillet et al. (2005) and a compilation of various types of galaxies from Krips et al. (2010). The  $^{12}\text{CO}(2-1)$  measurements presented in this paper have been corrected by a  $\text{CO } 2-1/1-0$  line ratio of 0.8, as measured in Melchior & Combes (2011) in a complex M31G within 10 and 30'' from the observed positions. The line indicates the best fit provided by Brouillet et al. (2005) for M31's main disc. Our points are systematically above the best fit they provide, suggesting an excess of  $\text{HCO}^+$ . The overall distribution of Krips et al. (2010) does not exhibit any clear pattern.

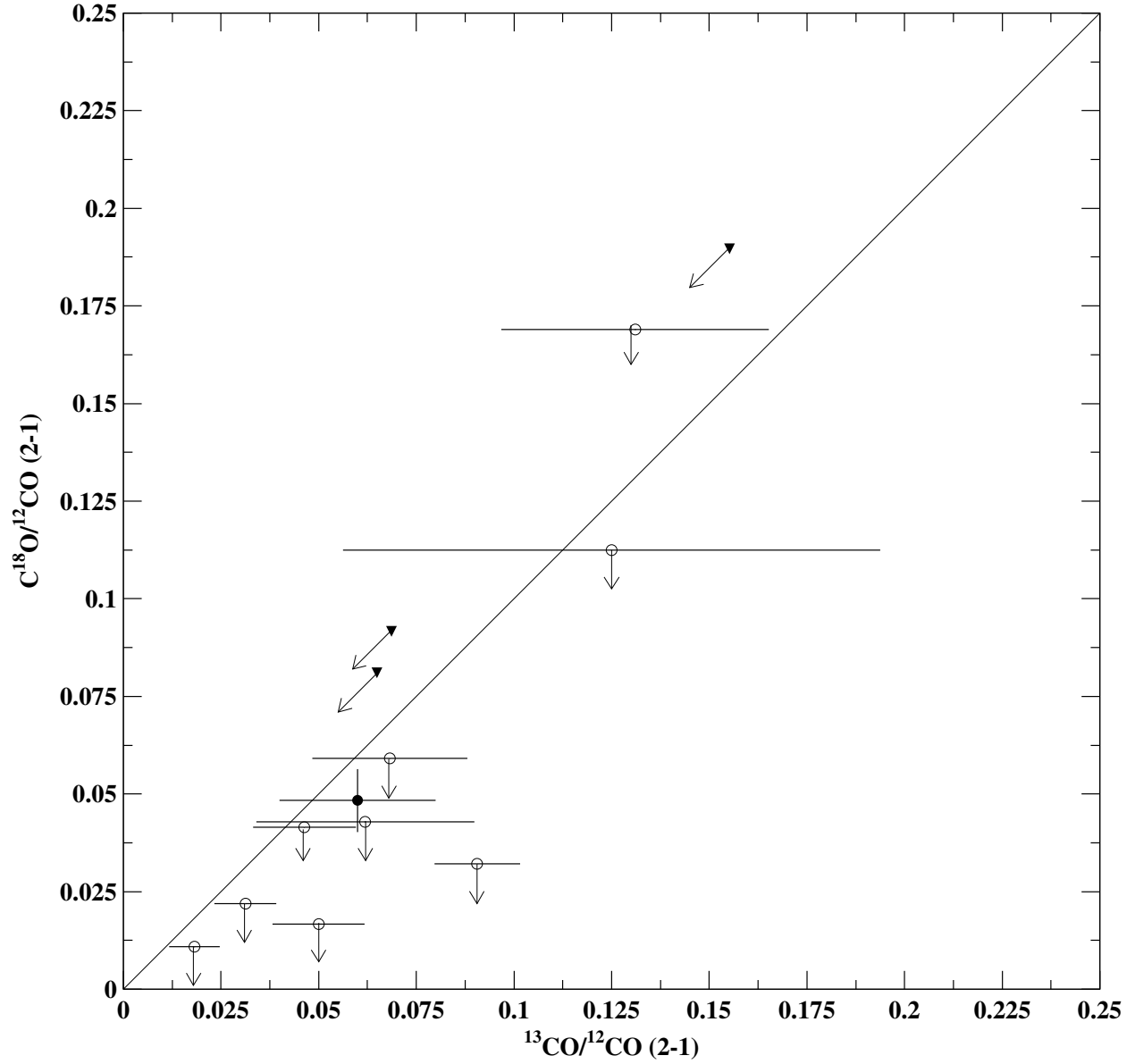


**Fig. A.3.**  $C^{18}O/^{12}CO$  (2-1) line ratios versus the  $^{13}CO/^{12}CO$  (2-1) line ratios presented in this paper. Arrows indicated  $3\sigma$  upper limits. The point with error bars our detection. The line indicates a slope 1.



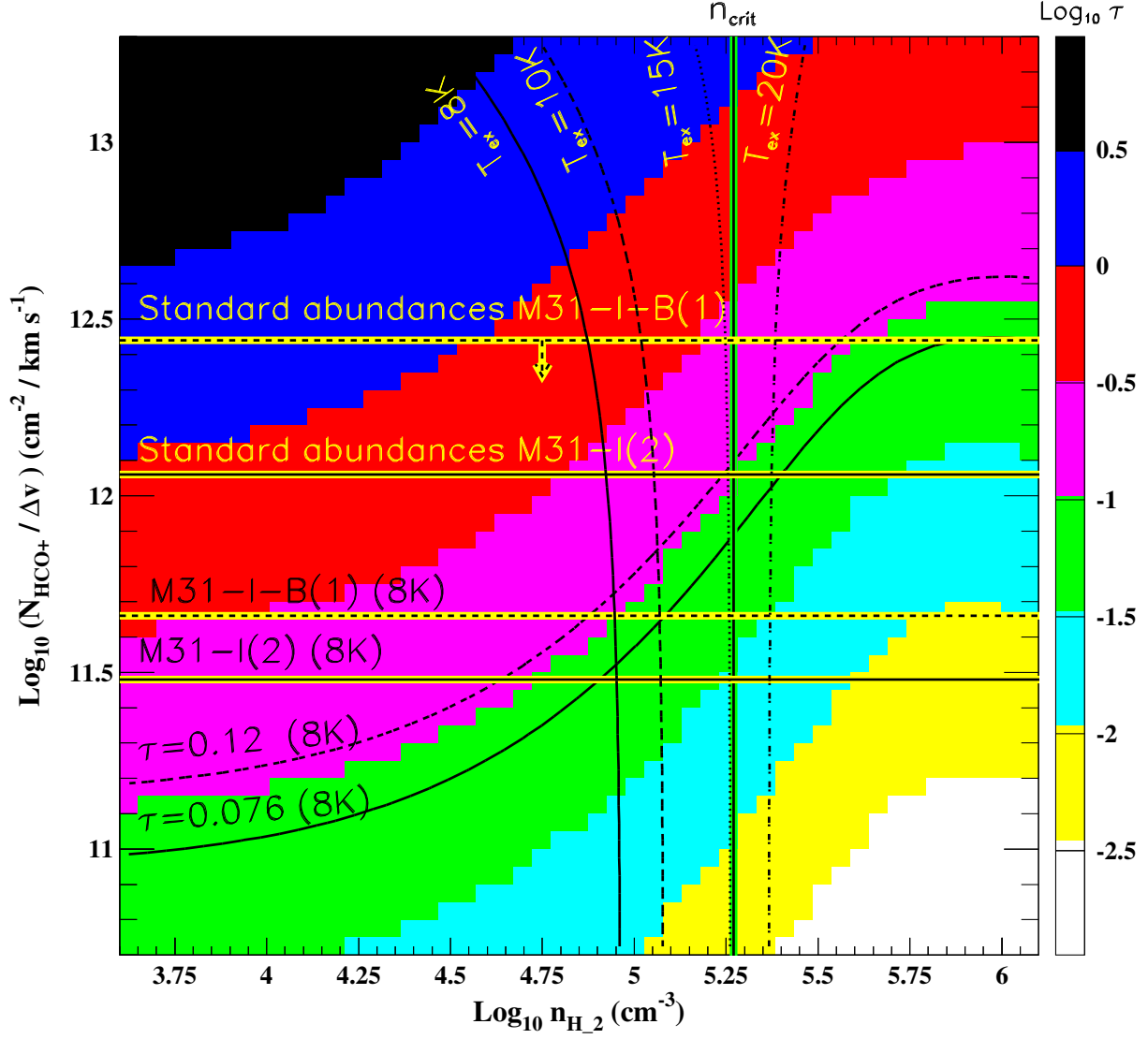


**Fig. A.4.** Main physical parameters corresponding to the HCO+(1-0) gas observed in M31-I(2) and M31-I-B(1). The optical depths are displayed as function of the HCO+(1-0) column density (per  $\text{km s}^{-1}$ ) and the molecular hydrogen density  $n_{\text{H}_2}$ . The vertical (green) line indicates the critical density computed for a collisional temperature of 20 K (see Table 3). The lower horizontal full (resp. dashed) lines displays column densities measured for M31-I(2) (resp. M31-I-B(1)) at 8 K. The upper horizontal lines correspond to the column densities computed with standard abundances (Bergin et al. 1995) and the corresponding molecular hydrogen column densities. For M31-I-B(1), we derive an upper limit as the molecular hydrogen column density is only available for a smaller beam (see Table 4) and we expect some dilution of the signal. The contour levels correspond to excitation temperatures of 10 K (full line), 15 K (dashed line), 20 K (dotted line) and 25 K (dash-dot line).